

Cloud Crushing and Dissipation of Uniformly-Driven Adiabatic Turbulence in Circumgalactic Media

ALEX LV ^{1,2} LILE WANG ^{1,2} RENYUE CEN ^{3,4} AND LUIS C. HO ^{1,2}

¹*Kavli Institute for Astronomy and Astrophysics, Peking University, Beijing 100871, People's Republic of China*

²*Department of Astronomy, School of Physics, Peking University, Beijing 100871, People's Republic of China*

³*Institute for Advanced Study in Physics, Zhejiang University, Hangzhou 310027, People's Republic of China*

⁴*Institute of Astronomy, School of Physics, Zhejiang University, Hangzhou 310027, People's Republic of China*

ABSTRACT

The circumgalactic medium (CGM) is responsive to kinetic disruptions generated by nearby astrophysical events. In this work, we study the saturation and dissipation of turbulent hydrodynamics within the CGM through an extensive array of 252 numerical simulations with a large parameter space. These simulations are endowed with proper cooling mechanisms to consistently explore the parameter space spanned by the average gas density, metallicity, and turbulence driving strength. A dichotomy emerges in the dynamics dissipation behaviors. Disturbances that are hot and subsonic are characterized by weak compression and slow dissipation, resulting in density fluctuations typically $\lesssim 10^{-2}$. Conversely, warm supersonic turbulence, marked by significant compression shocks and subsequent rapid cooling, is associated with substantial clumping factors $\sim 10^0 - 10^1$. In the supersonic cases, the kinetic energy decay is divided into a rate-limiting phase of shock dissipation and a comparatively swift phase of thermal dissipation, predominantly occurring within the overdense regions. Upon turbulence driving turnoff, the strong density contrasts decay within a relatively brief timescale of $\sim 30 - 300$ Myr, depending on the average gas density. Dense clouds are crushed on similar timescales of $\sim 30 - 100$ Myr, depending on turbulence driving strength but independent from average gas density. Results of this work also contribute a novel dataset of dissipation timescales that incorporates an understanding of kinematics and thermodynamics in addition to the traditional cooling rate tables, which may serve as a valuable asset for forthcoming simulations that aim to explore gas dynamics on galactic and cosmological scales.

Keywords: Circumgalactic medium (1879) — Collapsing clouds (267) — Hydrodynamical simulations (767) — Extragalactic astronomy (506)

1. INTRODUCTION

The circumgalactic medium (CGM) represents a rich, multiphased environment surrounding a galaxy, extending out up to the virial radius of the halo of $10^1 - 10^2$

kpc. It plays a crucial role in galaxy evolution, serving as an important source of baryons (Werk et al. 2014) for gas accretion onto the galactic disc. The physical state of the CGM can be split into distinct phases (Cen 2013): The cool phase of the CGM typically hovers around 10^4 to 10^5 K, while the hot phase 10^5 to 10^6 K (Rudie et al. 2012; Werk et al. 2013), meaning the bulk of the CGM consists of ionized gas. The mode of accretion depends heavily on the cooling timescale of the gas in relation to the freefall time: cold mode accretion characterized by filamentary streams and clumps when $t_{\text{cool}} < t_{\text{ff}}$ and hot mode accretion characterized by smooth cooling flows when $t_{\text{cool}} > t_{\text{ff}}$ (White & Rees 1978; Shen et al. 2013;

alexanderlu@stu.pku.edu.cn

Corresponding author: Lile Wang
lilew@pku.edu.cn

renyuecen@zju.edu.cn

lho.pku@gmail.com

(Crighton et al. 2013; Stern et al. 2020)). However, given the multiphased nature of the CGM, with varying metallicities, ionization states and temperatures, calculating and characterizing cooling timescales is a highly complex and nonlinear problem. Generally speaking, cooling streams only occur in the non-virialized regions of the circumgalactic medium where the accretion rate exceeds a critical threshold (Faucher-Giguère & Oh 2023). Thermal instabilities due to rapid cooling shocks the gas, leading to the formation of cold supersonic filaments (Balbus & Soker 1989; Dekel et al. 2009; Stern et al. 2021).

Unlike typical giant molecular cloud (GMC) conditions in the interstellar medium (ISM), in addition to being much hotter and mostly ionized, the CGM is also more diffuse. Observations reveal typical hydrogen column densities ranging from 10^{20} cm^{-2} near the disc down to 10^{14} cm^{-2} out to the virial radius (Werk et al. 2014), corresponding to number densities of around 10^{-2} to 10^{-3} cm^{-3} (Zahedy et al. 2019; Crighton et al. 2015). In such an environment, Jeans’ instabilities alone are insufficient in forming the cool phase of the CGM. Turbulence, evidenced by observations of broad line-widths (Werk et al. 2016; Rudie et al. 2012), plays a pivotal role in the gas dynamics of the CGM. A key driver in non-virialized halos with high accretion rates ($> 10 M_{\odot} \text{ yr}^{-1}$ for $10^{12} M_{\odot}$ haloes), as mentioned previously, are supersonic cool accretion flows which can stir turbulence via localized thermodynamics such as turbulent mixing between hot and cold phases and gas entrainment onto supersonic cold streams (Ji et al. 2019; Yang & Ji 2023). Internal feedback processes from supernovae and/or active galactic nuclei (AGN) within the galaxy, are also capable of driving turbulence in the CGM via large-scale outflows (Fielding et al. 2017). These feedback-induced turbulence motions in turn significantly impact the accretion of gas back onto the ISM or into the AGN, rendering it chaotic and asymmetric (Gaspari et al. 2013). They can also “stimulate” the clumping and eventual precipitation/accretion of CGM gas back onto the ISM in regimes where t_{cool} exceeds t_{ff} (Voit et al. 2017; Voit 2018). Within a cold cloud, turbulence may fragment the cloud into smaller “droplets”, exponentially increasing the surface area and growth rate of cool clumps (Gronke et al. 2022), which may explain the observational evidence for cold streams in the CGM. Additionally, turbulent winds can damp fluid instabilities in cool clouds in the presence of hot winds, stabilizing the cloud against destruction (Sparre et al. 2020), although compared to radiative cooling processes this only has a significant impact in highly supersonic flow (Li et al. 2020).

However, turbulence in such diffuse astrophysical media is not necessarily a continuous phenomenon, particularly in hot virialized haloes where accretion is subsonic and quasi-spherically symmetric (Faucher-Giguère & Oh 2023). Internal sources such as feedback are tied to episodic starburst and AGN activity from the disc (Rubin et al. 2014; Nielsen et al. 2015; Borthakur et al. 2013), and environmental sources are tied to episodic mergers or ram pressure on infall into a group or cluster. Hence, this necessitates the study of not merely steady-state turbulence driving, but also the dissipation of turbulence during quiescent periods. Using magnetohydrodynamic simulations of turbulence driving on molecular cloud scales with an isothermal equation of state, Stone et al. (1998) found saturation timescales to be independent of magnetic field strength, and energy dissipation timescales to be inversely correlated with magnetic field strength once turbulence was turned off. Magnetic fields provide magnetic pressure, which plays an important role in the gravitational stability of GMCs (Ostriker et al. 2001), although the role it plays in CGM cloud stability is uncertain and somewhat of an open question (Faucher-Giguère & Oh 2023). While Stone et al. (1998) considered variable magnetic field strength (damping strength) across multiple runs, they fixed their turbulence driving strength.

In this study, using hydrodynamic simulations, we investigate the effects of a generalized source of turbulence in a circumgalactic environment, though it can be extended to broader environments such as the intra-cluster medium or diffuse phases of the ISM. This work applies and builds on the methodology of Stone et al. (1998) to such environments, with variable turbulence driving strengths, an adiabatic equation of state and a standard collisional ionization equilibrium (CIE) cooling curve (Gnedin & Hollon 2012). We will elaborate on the methodological differences from Stone et al. (1998) in Section 2.

2. METHODS

2.1. Hydrodynamics and Thermodynamics

Studying turbulence numerically requires solving a consistent set of hydrodynamic equations. We employ the heterogeneous hydrodynamic code KRATOS (Wang et al. in prep), integrating the following Euler equations for an ideal gas:

$$\begin{aligned} \frac{\partial \rho}{\partial t} + \nabla \cdot (\rho \mathbf{v}) &= 0, \\ \frac{\partial (\rho \mathbf{v})}{\partial t} + \nabla \cdot (\rho \mathbf{v} \mathbf{v} + p \mathbf{I}) &= -\rho \nabla \Phi, \\ \frac{\partial \varepsilon}{\partial t} + \nabla \cdot [\mathbf{v}(\varepsilon + p)] &= -\rho \mathbf{v} \cdot \nabla \Phi + S. \end{aligned} \quad (1)$$

Here, ρ , \mathbf{v} , p and ϵ are the mass density, velocity, gas pressure, and total energy density, respectively. Φ is the gravitational potential, \mathbf{I} is the identity tensor, and S is the source term which captures additional thermodynamics beyond adiabatic compression and expansion. The hydrodynamic solver employs the slope-limited piecewise linear method (PLM) reconstruction scheme, the HLLC approximate Riemann solver, and the second order Runge-Kutta (RK2) time integrator. The Jeans length under typical CGM physical parameters approximately reads,

$$l_J \sim 10^4 \text{ pc} \times \left(\frac{T}{10^4 \text{ K}} \right)^{1/2} \left(\frac{\rho}{10^{-2} m_p \text{ cm}^{-3}} \right)^{-1/2}. \quad (2)$$

Such scales are considerably greater than the box size, let alone the typical cloud sizes, within our turbulent CGM simulations, making $\Phi \rightarrow 0$ a safe approximation in this study.

Within each sub-step in the RK2 cycles, we integrate the impact of S in every zone via a semi-implicit method. The cooling rate, represented by S in eq. (1), is based on the standard table from Gnedin & Hollon (2012). It covers the temperature range $10^3 - 10^8$ K and varying metallicities (see Figure 1). For typical CGM gases with density $\rho \lesssim 10^{-2} m_p \text{ cm}^{-3}$, the column density required for the cooling photons to escape in typical CGM scenarios is estimated by $N \lesssim 10^{19} \text{ cm}^{-2}$ per kpc along the escape path. For dense clouds with $\sim 10^2 \times$ the mean density, the typical sizes ($\sim 10^1$ pc) are sufficiently small to allow cooling photons to escape. These are sufficient to guarantee the optical-thin condition for the standard cooling table.

2.2. Turbulence Driving

This study focuses on the local dissipative behaviors of various phases of the CGM, hence the turbulence energy cascade is emulated via kinetic energy injection. We follow an approach similar to the one outlined in Mac Low (1999). During each timestep, the simulation domain is subject to a uniform perturbation via an acceleration vector aligned with a randomly selected direction vector \hat{a} . Denoting the amplitude of perturbation as A , the turbulence energy injection rate per by unit mass $\dot{\epsilon}_i$ (which will be referred to as turbulence driving strength) can be evaluated as,

$$\dot{\epsilon}_i = A \left\{ [\langle \rho \rangle L^3]^{-1} \Delta t \sum_{\mathbf{i}} \delta V_{\mathbf{i}} \rho_{\mathbf{i}} \mathbf{v}_{\mathbf{i}} \cdot \hat{a} \right\}, \quad (3)$$

where L is the box length, $\langle \rho \rangle$ is the mean mass density throughout the domain, and Δt is the current timestep. The summation goes through all cells, where \mathbf{i} is the

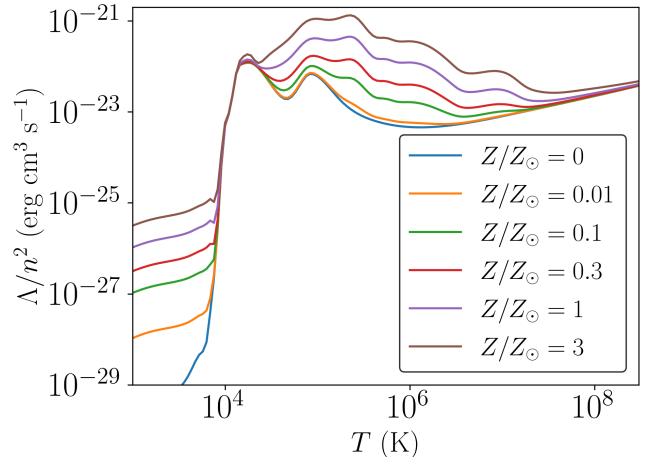


Figure 1. The cooling curves used in the simulations, adopting the data provided by Gnedin & Hollon (2012). The interpolated and extrapolated curves are computed as $\Lambda(Z/Z_{\odot})/n^2 = \Lambda(0)/n^2 + (Z/Z_{\odot})(\Lambda(1)/n^2 - \Lambda(0)/n^2)$.

cell index, and $\delta V_{\mathbf{i}}$, $\rho_{\mathbf{i}}$ and $\mathbf{v}_{\mathbf{i}}$ are the cell volume, mass density, and velocity vector for the \mathbf{i} -th cell. In practice, we establish a constant $\dot{\epsilon}_i$ as a key model parameter, which remains fixed throughout the simulation's progression up until turbulence turnoff. For each timestep, we utilize the enclosed summation in eq. (3) to normalize the amplitude A . Subsequently, we inject kinetic energy into the system by updating the velocity vector to $\mathbf{v}'_{\mathbf{i}} = \mathbf{v}_{\mathbf{i}} + A\hat{a}\Delta t$, and update the energy density accordingly.

2.3. Simulation Setup

Focusing on the local structures and characteristics of turbulence compression and subsequent dissipation processes, these simulations are conducted on $L = 256$ pc cubic domains with periodic boundary conditions. Various simulations are carried out to cover the parameter space, with 6 different metallicity values $Z/Z_{\odot} \in \{0, 0.01, 0.1, 0.3, 1, 3\}$, 6 different average gas density values $\langle \rho \rangle / (m_p \text{ cm}^{-3}) \in \{10^{-4}, 10^{-3}, 10^{-2}, 10^{-1}, 10^0, 10^1\}$, and 7 different turbulence energy injection rate values $\dot{\epsilon}_i / (\text{erg s}^{-1} \text{ g}^{-1}) \in \{0.01, 0.1, 0.3, 1, 3, 10, 100\}$. In total, there are 252 simulations. Selection of these parameters extend beyond the density and metallicity range typical of the CGM to account for denser, metal enriched phases captured in cool clouds, though we note that the Jeans length remains larger than our box even for our highest density runs.

Methodologically, setting aside the different astrophysical medium of interest and our exclusion of magnetic fields, a key difference between this work and Stone et al. (1998) is our usage of an adiabatic equation of state with the inclusion of thermal energy, adiabatic heating

and a radiative cooling function. This is necessary given the differences between CGM and GMC environments: the CGM is orders of magnitude hotter and reside in efficient cooling temperature regimes, and is subject to much more violent turbulence driving events. Without artificial viscosity, energy dissipation happens entirely via the radiative cooling function, with kinetic energy dissipating via the energy cascade into thermal energy.

The wide coverage over the multi-dimensional parameter space limits the viable resolution of each run due to computational and storage limits. We adopt a relatively low 128^3 resolution for each run, resulting in a spatial resolution of 2 pc. Such resolution is sufficient to resolve compressive shocks that form relatively dense gas clumps with sizes ~ 10 pc (see Section 3.6). For conditions matching more closely to those of the dense phase of the CGM, namely $Z/Z_\odot \in \{0.1, 0.3\}$ and $\rho/(m_p \text{ cm}^{-3}) \in \{10^{-2}, 10^{-1}\}$, we run an additional set of higher resolution 256^3 runs with the exact same setup otherwise. The denser and higher metallicity phases are chosen given their efficient cooling regimes, which allows the turbulence to remain supersonic for higher values of $\dot{\epsilon}_i$, and thus more analyzable high resolution runs.

The initial conditions of each run are set so that the initial gas temperature is uniformly $T = 3 \times 10^4$ K.

The initial velocity field is randomized, with each component of each cell's velocity having a random value between $\pm 1 \text{ km s}^{-1}$, representing a homogenous gas with initial subsonic motions. The choice of initial velocity field is arbitrary as long as the velocities are subsonic, since all runs will undergo turbulence driving until the gas reaches saturated steady-state turbulence. An initial non-zero velocity field is necessary, since given a periodic box and entirely uniform perturbations, theoretically no substructures would form, and any resulting substructures that do form are the result of numerical errors and approximations in the flux advection and reconstruction schemes. The randomized subsonic initial motions guarantee a physical basis for any resulting turbulence driven substructures.

Each run is fixed to 210000 cycles. Turbulence driving is turned on for the first 200000 cycles to guarantee turbulence saturation and a turbulent quasi-steady states. Turbulence is turned off for the last 10000 cycles to study the dissipation of turbulences. This scheme of fixing the number of cycles is related to the Courant-Friedrichs-Lewy (CFL) conditions, which limits the timestep of each cycle Δt by

$$\Delta t = C \times \min_i \left\{ \frac{\Delta x}{|\mathbf{v}_i| + c_{s,i}} \right\}. \quad (4)$$

In this work we choose $C = 0.3$. As one can easily deduce, each cycle with timestep constrained by eq. (4) represents a fraction of the fluid crossing time (in case of high Mach numbers) or sound crossing time (in case of low Mach numbers). Therefore, a fixed number of cycles naturally covers a similar number of fluid or sound crossing timescales, providing sufficient temporal resolution for analysis while minimizing data storage requirements.

3. RESULTS

Unless specified otherwise, plots showing a sample of data use the 128^3 runs, while plots showing single representative samples use the 256^3 runs. Plots showing 256^3 runs will have this fact relayed in figure captions, and we will discuss resolution convergence in Appendix A.

3.1. Subsonic and Supersonic Dissipation

A bimodality in the initial turbulent state and the energy dissipation is seen in Figure 2, with a distinct supersonic and subsonic turbulence regime. In the subsonic case, the initial averaged mach numbers (\mathcal{M}) are less than 1, the initial temperatures are above 10^6 K, and little dissipation is present within $3t_s$. Meanwhile in the supersonic case, the \mathcal{M} values are of order unity and above, the initial temperatures are below 10^5 K, and significant energy dissipation of 10 – 80% within three kinetic saturation timescales is present within $3t_s$. There is a temperature gradient across the supersonic runs, where hotter steady-state turbulence leads to increased energy dissipation. Among the subsonic runs, the energy loss hovers around 1%, but runs with $\dot{\epsilon}_i = 100 \text{ erg s}^{-1} \text{ g}^{-1}$ and initial temperatures of around 10^8 K lose around 3 – 6% of their initial energy within $3t_s$, with initial \mathcal{M} higher than the other subsonic runs. The distribution of fractional energy losses almost seems multimodal, with two distinct subsonic regimes and one distinct supersonic regime. Across runs with fixed initial conditions (same n and Z/Z_\odot), increasing $\dot{\epsilon}_i$ leads to an eventual transition point from supersonic to subsonic turbulence (see Figure 3, though this offset in both \mathcal{M} and $\Delta\epsilon/\epsilon_0$ between the subsonic $\dot{\epsilon}_i = 100 \text{ erg s}^{-1} \text{ g}^{-1}$ and other subsonic runs may imply that with even stronger turbulence driving there is another supersonic regime. The transition occurs when thermal dissipation via radiative cooling is unable to reach an equilibrium with energy injection via turbulence driving and energy cascade until the gas temperature exceeds 10^7 K and enters the bremsstrahlung regime. Regions along the cooling curve (see Figure 1) where $\partial\Lambda/\partial T < 0$ are unstable during turbulence driving, hence giving rise to a temperature (and by proxy the subsonic/supersonic turbulence) bimodality.

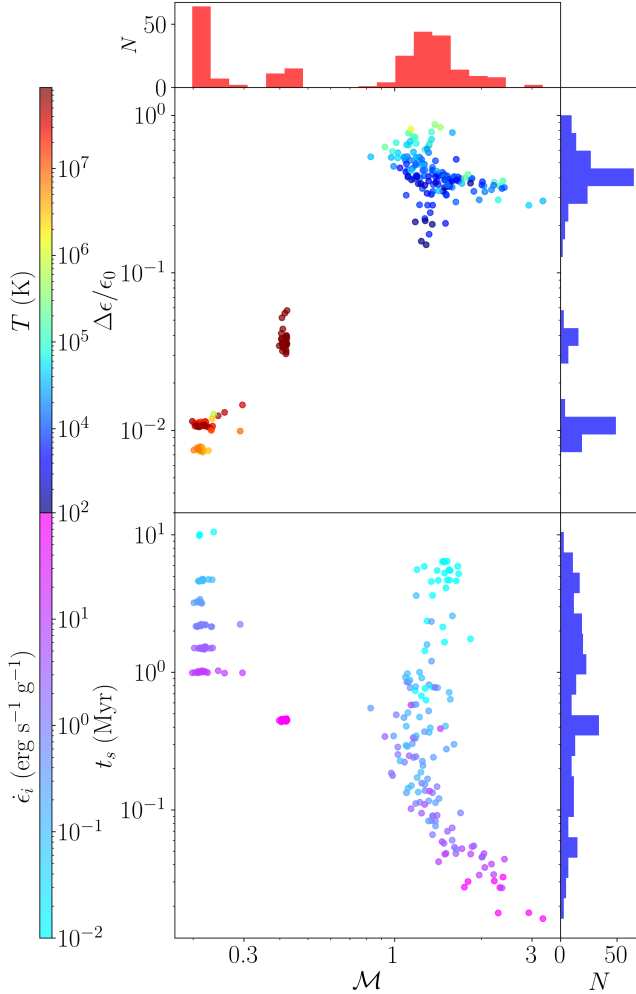


Figure 2. Two scatter plots showing the mass averaged Mach number (\mathcal{M}) vs the fractional energy decay at three saturation times ($\Delta\epsilon/\epsilon_0$) on top and the kinetic energy saturation time (t_s) on the bottom, with each point representing a run. \mathcal{M} is defined as $v_{\text{avg}}/c_{s,0}$, where v_{avg} is the mass averaged velocity across all cells and the initial sound speed $c_{s,0}$ is computed from the mass-averaged temperature of the entire box. t_s represents the kinetic energy saturation time defined as the ratio of the kinetic specific energy to the turbulence driving strength $t_s = \epsilon_k/\dot{\epsilon}_i$. The temperatures on the top plot represent initial temperatures at turbulence turnoff.

Examining the distribution of kinetic saturation times, which is defined as $t_s = \epsilon_k/\dot{\epsilon}_i$ during steady state turbulence, we observe it to be smooth and continuous among the supersonic runs, with timescales ranging from $3 \times 10^{-2} - 10^1$ Myr. As with temperature, we see a $\dot{\epsilon}_i$ gradient where stronger turbulence driving leads to lower t_s . \mathcal{M} also shows a peculiar trend where it scales positively with $\dot{\epsilon}_i$ for $t_s > 3 \times 10^{-1}$ Myr, but negatively with $\dot{\epsilon}_i$ for $t_s < 3 \times 10^{-1}$ Myr. The subsonic runs appear clustered, with distinct vertical offsets in t_s congruent to distinct values of $\dot{\epsilon}_i$, which is far different from the

continuous distribution of t_s among the supersonic runs. This would suggest in the subsonic regime, t_s depends primarily on $\dot{\epsilon}_i$, with weaker dependencies (if any) on n or Z .

The physical distinction between subsonic and supersonic dissipation becomes clearer in Figure 3, where we examine the steady state of two particular 256^3 resolution runs in more detail. On the top where $\dot{\epsilon}_i = 1 \text{ erg s}^{-1} \text{g}^{-1}$, we observe large variations in ρ and T across many orders of magnitude, and distinct overdense clumps in the gas. Meanwhile on the bottom, where $\dot{\epsilon}_i = 3 \text{ erg s}^{-1} \text{g}^{-1}$, we observe a near uniform gas with perturbations of order unity. Subsonic motions in the gas are unable to produce shocks, which is a prerequisite for substructure formation in diffuse, non self-gravitating regimes. The right column paints a clearer picture of the different regimes of dissipation seen in Figure 2. Supersonic turbulence sees two distinct epochs of dissipation, characterized by an initial rapid dissipation epoch followed by a slow dissipation epoch. Subsonic turbulence on the other hand, sees only a slow dissipation epoch, cotemporal with an increase in thermal energy. This increase can also be seen in thermal energy of the supersonic run, and represents the cascading rate of kinetic energy into thermal energy via numerical hydrodynamic processes exceeding the radiative cooling rate. The physical nature behind the two dissipation epochs and the individual dissipative behaviours of thermal and kinetic energy will be examined more closely in Section 3.2.

This distinction between the dissipation rates of supersonic and subsonic turbulence can be seen in Figure 4. Here the energy is normalized by the initial sound speed at turbulence turnoff $c_{s,0}^2$ consistent with Stone et al. (1998). The normalized dissipation rates of the supersonic runs as a whole are a full dex higher than those of the subsonic runs up to a few t_s , beyond which the rates begin to converge. The convergence is indicative of the dissipation of supersonic motions and dispersal of substructures as the box becomes homogenized, and is discussed more in depth in the following sections. Figure 4 encapsulates most of the entire range in t_s spanned by the subsonic runs, with the supersonic runs spanning a larger range up to hundreds and thousands of t_s . As mentioned earlier, this is the result of the shorter timesteps of the subsonic runs.

3.2. Thermal vs Kinetic Supersonic Dissipation

Fixing our attention towards the supersonic runs, Figure 5 shows the time evolution of specific thermal (ϵ_g) and kinetic (ϵ_k) energy binned in $\dot{\epsilon}_i$, with the top two plots normalized by initial sound speed $c_{s,0}^2$ at turbu-

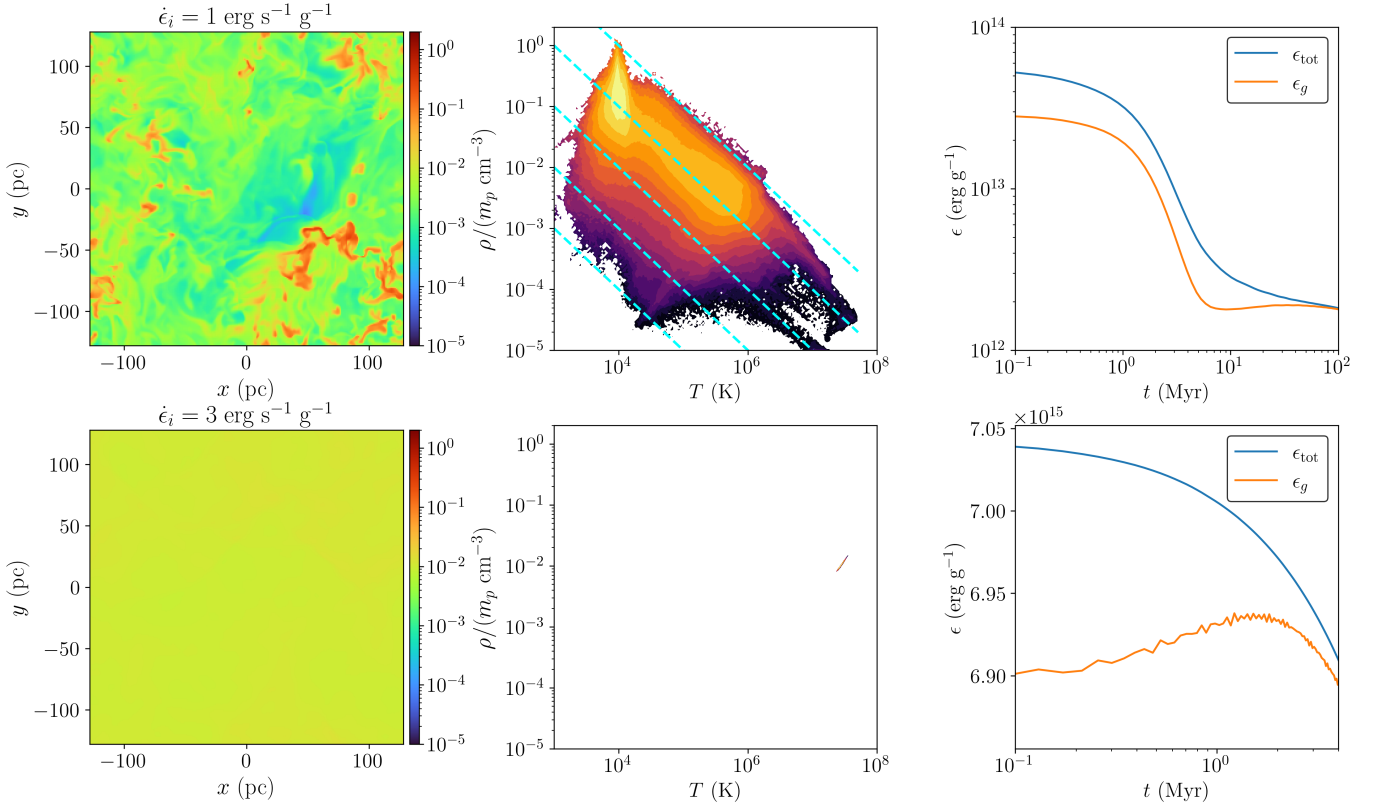


Figure 3. A comparison between two 256^3 resolution runs where $Z/Z_\odot = 0.3$ and $n = 10^{-2} \text{ cm}^{-3}$, with the top and bottom rows representing $\dot{\epsilon}_i = 1 \text{ erg s}^{-1} \text{ g}^{-1}$ and $\dot{\epsilon}_i = 3 \text{ erg s}^{-1} \text{ g}^{-1}$ respectively. The left column shows density slice plots at $z = 0$, the middle column the mass-weighted density-temperature phase plots (contoured 2D histogram), and the right column the specific total and thermal energies and the mass-averaged temperature over time. The dotted blue lines in the top middle phase plot represent lines of constant pressure.

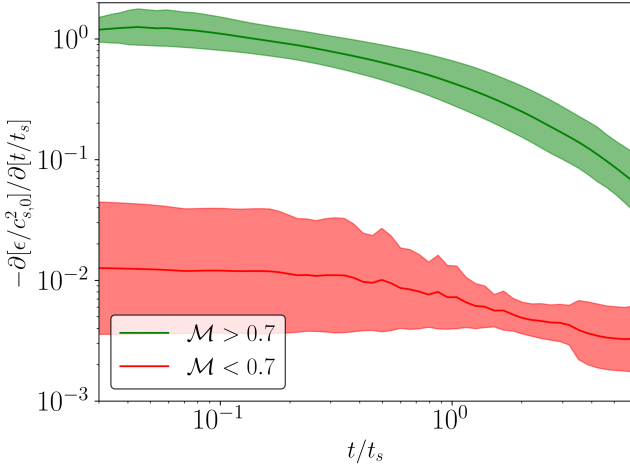


Figure 4. The dissipation rate of specific total energy, normalized by initial sound speed $c_{s,0}^2$, over time for supersonic (green) and subsonic runs (red). \mathcal{M} follows the same definition as the one in Figure 2, which is $v_{\text{avg}}/c_{s,0}$, and t_s represent the kinetic energy saturation time. The shaded error regions represent 1σ .

lence turnoff and t_s . It is immediately clear that ϵ_g and

ϵ_k dissipate very differently on very different timescales. In the normalized plots, there are significant variations in thermal dissipative behaviour with respect to $\dot{\epsilon}_i$. Beyond $10t_s$, 1 dex increases in $\dot{\epsilon}_i$ result in an approximate 0.5 dex drop in normalized thermal energy. Meanwhile, kinetic dissipation curves are more or less within each others' error regions, although there is some weak dependancy on $\dot{\epsilon}_i$, with stronger turbulence driving leading to slightly shorter dissipation timescales relative to t_s .

Thermal dissipation is characterized by the initial rapid dissipation epoch as previously seen in Figure 3, on timescales of order $0.1t_s$. The separation between different binned values of $\dot{\epsilon}_i$ is somewhat orderly in the normalized plot, manifesting themselves as a "branch-off" from their universal initial values of $c_{s,0}^2/(\gamma - 1)$ starting at $0.01t_s$. Higher $\dot{\epsilon}_i$ sees higher amounts of normalized thermal dissipation during the rapid epoch, before all runs eventually see dissipation rates decreasing significantly and their curves flattening. The bottom unnormalized thermal dissipation plot reveals a degree of non-linearity in the starting times of the rapid dissipation epoch with the $\dot{\epsilon}_i = 10 \text{ erg s}^{-1} \text{ g}^{-1}$ beginning

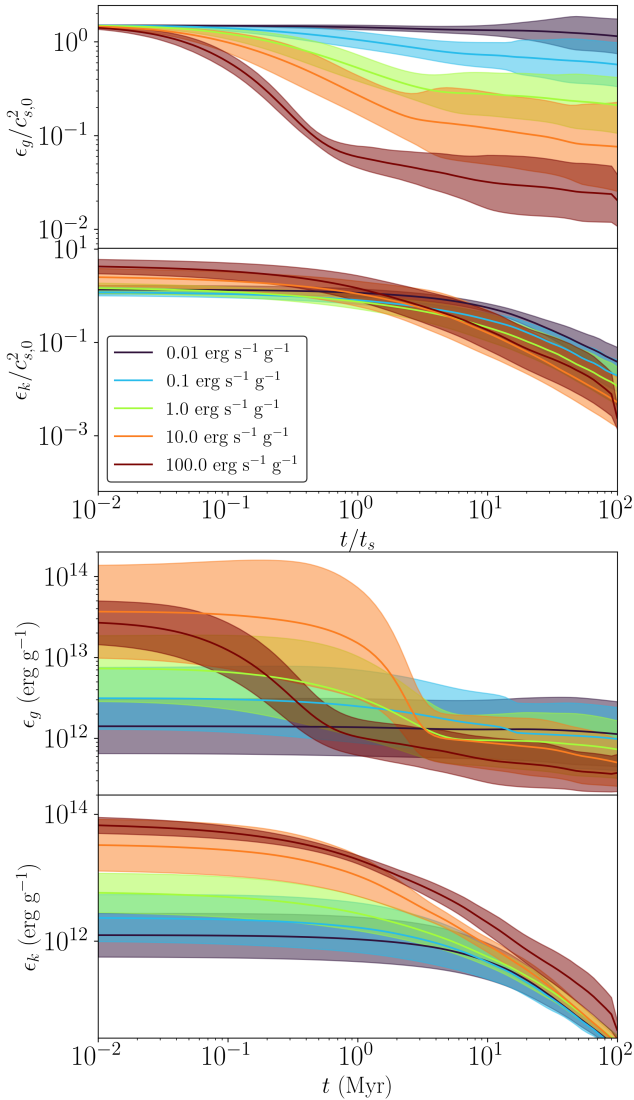


Figure 5. Normalized (top two) and unnormalized (bottom two) energy dissipation curves over time. Specific energy is normalized by initial sound speed $c_{s,0}^2$, and time is normalized by kinetic saturation time t_s . The shaded regions represent 1σ error regions and each coloured curve represents different values of $\dot{\epsilon}_i$. The first and third plots show thermal energy, and the second and fourth plots show kinetic energy.

at later times compared to the other runs. The unnormalized plot also reveals a range of energy plateaus shared across all runs afterwards, representing an inefficient cooling regime once the gas has reached 10^4 K, and will be examined in more detail in Figures 6 and 7. Kinetic dissipation is characterized by a steady exponential drop over time. Unlike thermal dissipation, kinetic dissipation is far more weakly coupled to $\dot{\epsilon}_i$, despite the kinetic energy during steady state turbulence having a strong dependency on $\dot{\epsilon}_i$ as seen in the initial values of the kinetic dissipation plots, both normalized

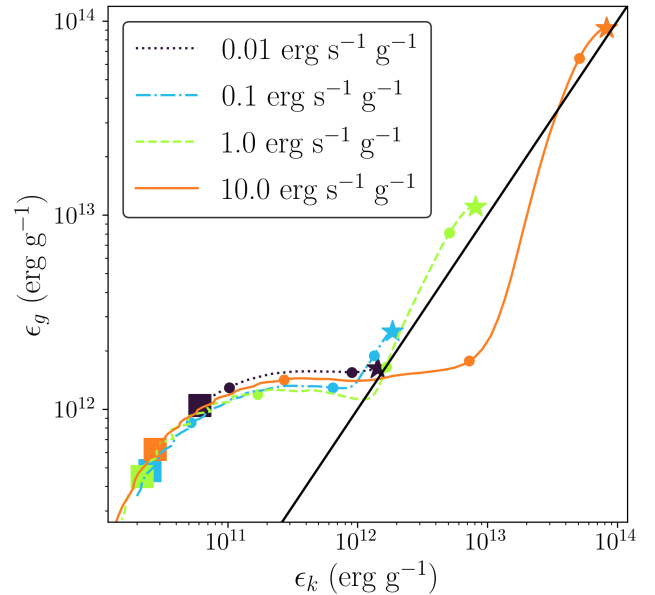


Figure 6. Phase plots showing the time tracks of thermal versus kinetic energy for 256^3 resolution runs corresponding to $Z/Z_\odot = 0.3$ and $n = 0.1 \text{ cm}^{-3}$. Stars denote the turbulence driving turn off time where each curve begins, circular dots denote t_s , $10t_s$ and $100t_s$ as one moves from the star and along the curve, and the squares denote $t = 100 \text{ Myr}$. The black line represents the $x = y$ line.

and unnormalized. In the unnormalized plot, despite the gradient of initial ϵ_k , the dissipation curves all converge after 100 Myr.

We show the time tracks of a few higher resolution runs comparing thermal and kinetic energy directly in Figure 6. We observe rapid dissipation in thermal energy within the first $10t_s$ for higher values of $\dot{\epsilon}_i$, and relatively consistent exponential kinetic dissipation rate with no plateaus, consistent with our observations of Figure 5. The latter can be further evidenced by the approximately even horizontal spacing between circles (most pronounced for $\dot{\epsilon}_i = 10 \text{ erg s}^{-1} \text{ g}^{-1}$), with ϵ_k being a viable proxy for time. We also confirm the convergence of kinetic and thermal energy as seen in the unnormalized bottom plots of Figure 5 - regardless of initial energy or turbulence driving strength, for $t > 30t_s$ the dissipation curves overlap. Additionally, the squares which mark $t = 100 \text{ Myr}$ are more or less at the same location across all four runs where the kinetic and thermal dissipation curves have overlapped. This would suggest 100 Myr to be a "universal" turbulence dissipation timescale, depending on n and Z but fully independent from $\dot{\epsilon}_i$. This independence will also be explored further in Section 3.5 on the dissipation of overdensities. The overlap also coincides with a plateau in thermal energy, formed by a combination of inefficient cooling as the gas

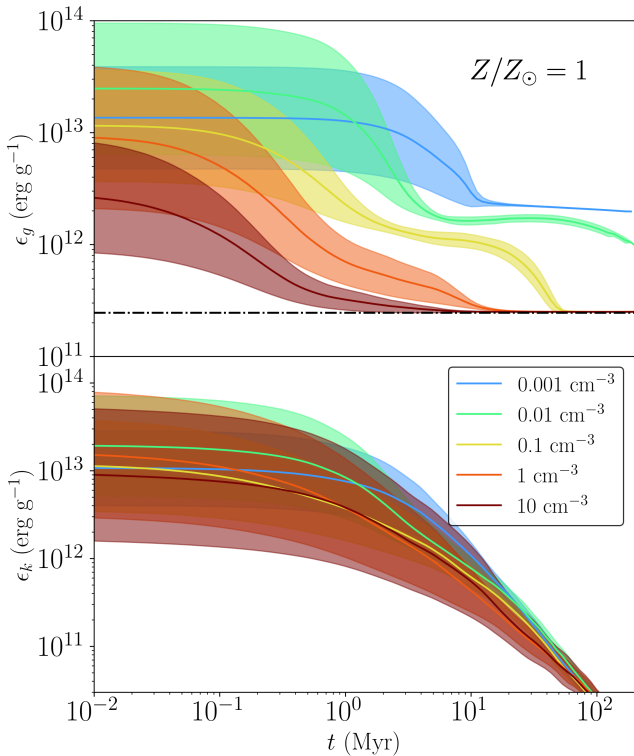


Figure 7. A similar plot as Figure 5 but with curves binned in n as opposed to ϵ_i . The shaded regions represent 1σ . The thermal energy (top) plot shows only $Z/Z_\odot = 1$ runs with the shaded regions only representing variations in ϵ_i , while the kinetic energy (bottom) plot shows all metallicity runs with the shaded regions representing variations in both Z and ϵ_i . The black dotted line represents the specific thermal energy floor corresponding to the 1000 K temperature floor.

reaches 10^4 K and the continuous cascade from kinetic to thermal energy.

We observe variations in the end state with respect to initial conditions in Figure 7, with all quantities unnormalized and curves separated by number density. The top thermal energy plot affirms the convergence of thermal energy curves observed in Figure 6 across a larger, lower resolution sample size, with varied turbulence driving across fixed initial conditions. Since the metallicity is fixed, the spread within each n bin represents only variations in ϵ_i . We denote the temperature floor with the black dotted line as an unphysical asymptote the thermal energy approaches across all runs, but as seen in Figure 1, the cooling rates drop by many orders of magnitude below 10^4 K, so the actual physical evolution of thermal energy would not be a significant downwards deviation from a horizontal asymptote. We see that this convergence is independent of turbulence driving as the error regions decrease in size, and the value of ϵ_g at which the convergence begins, depends on n and Z (since inefficient cooling can also arise from

low n and/or low Z). We also affirm that these convergences occur at thermal energy plateaus after the initial rapid dissipation epoch. Kinetic energy, as with Figure 6 and Figure 5 also shows convergence and overlap. This convergence and overlap via binning both in n and in ϵ_i , suggests a universal kinetic energy dissipation timescale. We note that this convergence point is at 100 Myr in both Figures 5 and 7, the same location marked by the squares in Figure 6.

The spatial scaling of the turbulence can be analyzed via the turbulence power spectrum (Bavassano et al. 1982; Burkhart et al. 2015; Bustard & Oh 2023), shown in Figure 8. We compute the turbulence power spectra as follows:

$$P_k(k) = \frac{1}{2}k^2 \int d\Omega_k |\hat{v}(\vec{k})|^2 \quad (5)$$

where $\int d\Omega_k$ represents a solid angle integral over k -space, and k represents the radial component of \vec{k} . $\hat{v}(\vec{k})$ represents the Fourier Transform (FT) of the velocity field:

$$\hat{v}(\vec{k}) = \frac{1}{(2\pi)^3} \int \vec{v}(\vec{r}) e^{-i\vec{k}\cdot\vec{r}} d^3r \quad (6)$$

The factor of $1/2$ in eq. (5) represents the conversion from velocity-squared to specific kinetic energy.

The dissipation is visible in the downward shift in the power spectra in the bottom plot, with relatively even spacing between the power spectra at t_s , $10t_s$ and $100t_s$. The upwards bump at higher k along the inertial regimes shows the bottleneck effect (Dobler et al. 2003; Donzis & Sreenivasan 2010), representing a buildup of energy below the dissipation range. The inertial regimes of our runs match the kolmogorov $k^{-5/3}$ power law (Kolmogorov 1941) fairly well, both during and after steady state turbulence. This is indicative of the weakly supersonic nature of our runs with \mathcal{M} only being on order unity (Ossenkopf & Mac Low 2002; Larson 1981). Notably, stronger turbulence driving does not lead to an increasingly shocked gas with a k^{-2} power law (Burgers 1948), but rather a near-congruent upwards shift in the entire spectrum. The shape of the spectrum remains preserved during dissipation, consistent with (Vazza et al. 2009).

3.3. Comparisons with Isothermal, Compressible GMC Dissipation

We compare our dissipation curves with various kinetic dissipation curves in GMCs in Figure 9. The black curve from Stone et al. (1998) serves as a fiducial comparison representing dissipation with pure hydrodynamics without magnetic fields or self gravity. Two key distinctions emerge - as also seen in Figure 2 our supersonic

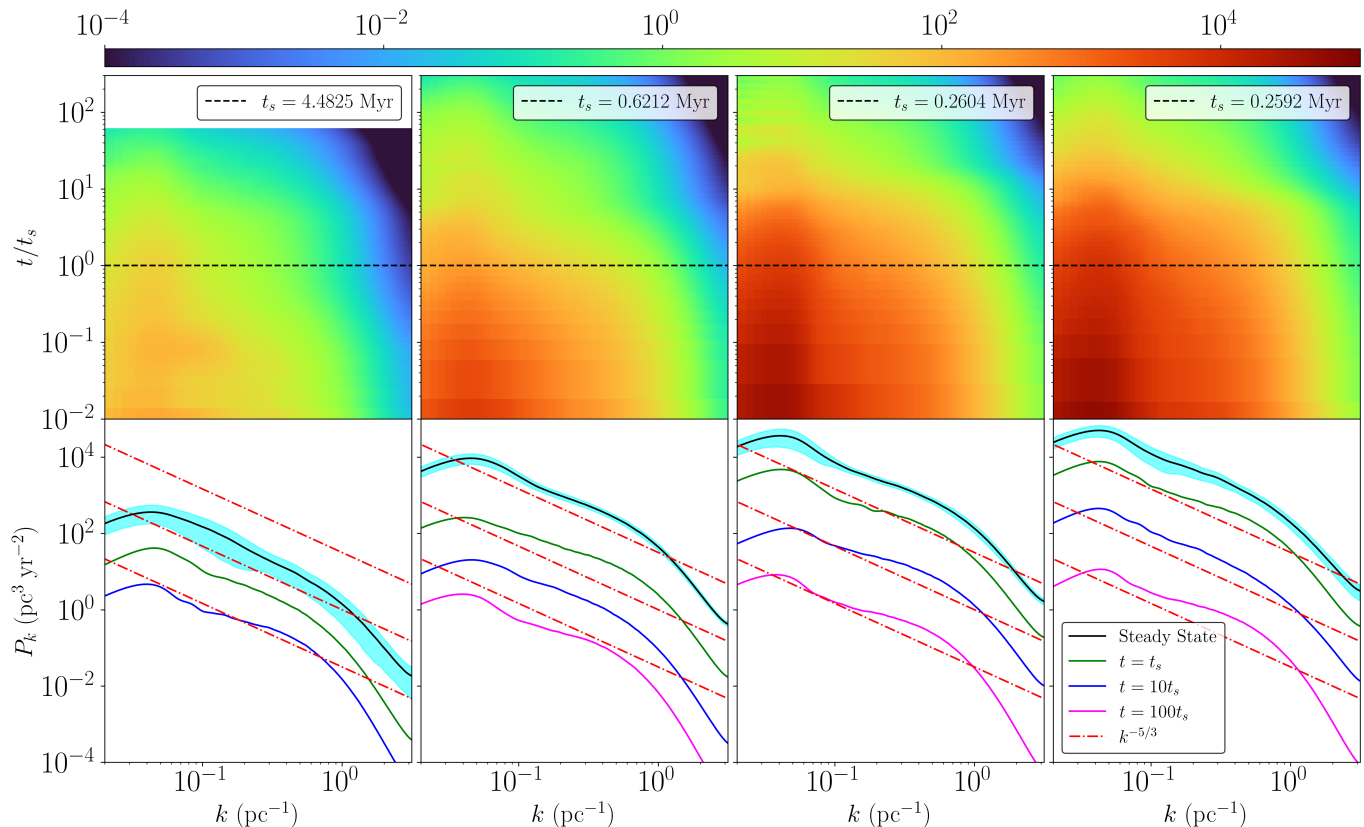


Figure 8. The turbulence power spectra of the four high resolution 256^3 runs shown in Figure 6, where $Z/Z_\odot = 0.3$ and $n = 0.1 \text{ cm}^{-3}$, and $\dot{\epsilon}_i$ being 0.01, 0.1, 1.0 and 10.0 $\text{erg s}^{-1} \text{g}^{-1}$ from left to right. The bottom row plots the turbulence power spectra during steady state turbulence, after t_s , $10t_s$ and $100t_s$, as well as $k^{-5/3}$ reference lines representing the inertial regime of the kolmogorov spectrum. The cyan coloured region represents 1σ across the last twenty outputs of the steady state turbulence epoch. The top row plots the power spectra from turbulence turn off up to $100t_s$, with the colour denoting ϵ_k . The value of t_s is also shown across each of the four runs. Both the top and bottom row plots are smoothed using degree-5 polynomial splines for visualization purposes. The leftmost $\dot{\epsilon}_i = 0.01 \text{ erg s}^{-1} \text{g}^{-1}$ column does not show a $100t_s$ power spectrum since the simulation run ended before $100t_s$.

runs are only weakly supersonic with M on order unity, while Stone et al. (1998) sees stronger supersonic motions with M being an order of magnitude higher. The dissipation timescales are also significantly shorter relative to t_s , where kinetic energy dissipates well within t_s while for our runs both thermal and kinetic energy dissipate on timescales greater than $10t_s$. Both distinctions are reflective of the different astrophysical medium of interest (GMCs are much cooler than CGMs, which allows significantly weaker velocity perturbations to drive stronger supersonic turbulent motions) and of the different physical processes through which dissipation occurs (energy cascade and radiative cooling for us, artificial viscosity for Stone et al. (1998)). The cyan and magenta curves from Ostriker et al. (1999) and Ostriker et al. (2001) illustrate the effects of self gravity (both) and magnetic fields (latter). While they play a minor role in stabilization against dissipation, their dissipation timescales remain well within t_s .

We note that the artificial viscosity employed by the aforementioned authors via the code ZEUS (Stone & Norman 1992a) is necessary to capture and thermalize shocks, while KRATOS adopts higher order Godunov solver. Physically, in our work, kinetic dissipation occurs only via shock thermalization through adiabatic compression. Numerical viscosity also plays a role in shock thermalization (Nelson et al. 2013), though its effects diminish with more accurate solvers and higher resolution grids (Zhang et al. 2003). Harkening back to Figure 8, it's likely that the bottleneck (Dobler et al. 2003) is the result of both a lack of subgrid viscous forces accounting for dissipation at kolmogorov microscales, and insufficient numerical viscosity given our numerical scheme and resolution.

3.4. Energy Dissipation Timescales

We quantify the raw dissipation timescales t_h in Figure 10, defined as the time it takes for the total, thermal or kinetic energy to drop by half. The primary trend on

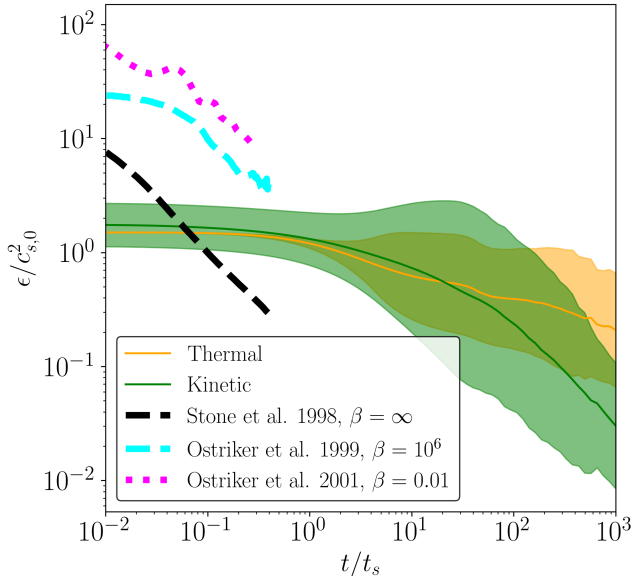


Figure 9. A comparison between our thermal and kinetic dissipation curves and the kinetic dissipation curves of Stone et al. (1998) (black), Ostriker et al. (1999) (cyan) and Ostriker et al. (2001) (magenta). The latter three curves show dissipation under artificial viscosity, an isothermal equation of state and the presence of magnetic fields where $B = \beta^{-1/2} \times 1.4 (T/10 \text{ K})^{1/2} (n/10^2 \text{ cm}^{-3}) \mu\text{G}$ (so $\beta = \infty$ represents pure hydrodynamics). The cyan and magenta dissipation curves include self-gravity. t_s represents the kinetic energy saturation time defined as $\epsilon_k/\dot{\epsilon}_i$ during steady state turbulence, and the energies are normalized by sound speed squared $c_{s,0}^2$ right at turbulence driving turnoff.

the top plot shows decreasing dissipation timescales with increasing $\dot{\epsilon}_i$ across all metallicities, with some n dependence for higher metallicities particularly at $Z/Z_\odot = 1$ and $Z/Z_\odot = 3$. There is little discernible correlation between the dissipation timescale and metallicity - rather, increased metallicity leads to enhanced cooling, allowing for some runs to reach the supersonic regime which would have been subsonic at lower metallicities, as seen with the increased number of supersonic runs above the diagonal for higher metallicity contour plots. On the middle and bottom plots, we can affirm our earlier observations from Section 3.2. Noting that blank bins below the diagonal in the thermal dissipation timescale represent supersonic runs that could not dissipate half their thermal energy over the simulation and interpreting those bins as having longer dissipation timescales, we see a steep drop in t_h with increased $\dot{\epsilon}_i$ and n of several orders of magnitude. Meanwhile in the bottom plot, while a $\dot{\epsilon}_i$ dependence in the kinetic dissipation timescales can be observed, it is far less steep and spans fewer orders of magnitude compared to the thermal dissipation timescales. No clear n dependence can be ob-

served either. The subsonic runs occupy the top left regions of all plots, above the diagonal, representing initial parameters where cooling is insufficient in preventing the gas from reaching a hot subsonic turbulent state.

We also present a set of dimensionless dissipation timescales in Figure 11. We define a kinetic timescale in $t_{\text{cross},0} = \ell/\langle v_{\text{rms}} \rangle$ and a thermal timescale in $t_{\text{cool},0} = E_{g,0}/\sum_i n_i^2 \Lambda(T_i) \Delta x_i^3$. The former represents the initial crossing time at turbulence turnoff, where $\langle v_{\text{rms}} \rangle$ represents the mass averaged rms velocity across every cell, while the latter represents the initial cooling time at turbulence turnoff, where $E_{g,0}$ represents the total initial thermal energy and the denominator represents the total cooling rate integrated across every cell. Subsonic kinetic dissipation shows a universal dimensionless timescale of approximately $0.6t_{\text{cross},0}$, while supersonic thermal dissipation shows a convergence towards a universal dimensionless timescale of roughly $8.5t_{\text{cool},0}$.

3.5. Density Homogenization

As seen in Figure 3 and as discussed in previous sections, there are density contrasts spanning multiple orders of magnitude during steady state turbulence. We define overall scale of such density contrasts via the clumping factor, which is defined as $C = \langle \rho^2 \rangle / \langle \rho \rangle^2$, where $\langle \rho \rangle$ represents a spatial average across all cells. We can examine the broad density homogenization of the medium via dissipation in the clumping factor. We label the full definition of C in subsequent plots and figures for clarity, and plot $C - 1$ given $C = 1$ represents a completely uniform medium.

We show the time evolution of C in Figure 12 with respect to both $\dot{\epsilon}_i$ and n . An expected observation of the top plot shows a positive correlation between $\dot{\epsilon}_i$ and steady state clumping, as well as a significant valley between the clumping factors of subsonic and supersonic runs. Subsonic clumping factors do show a decrease of around a single dex, although this is insignificant compared to the several-dex decreases in the C of the supersonic runs, especially when considering the -1 shift in the y axis. We define a supersonic turbulent medium to be homogenized if its clumping factor falls below a density homogenization limit of $C_{\text{sub}} \approx 1.0132$ representing 5σ from the mean initial subsonic clumping factor. Functionally, this definition translates to a density homogenization timescale t_{Diss}^C , beyond which the density contrasts of a dissipated supersonic turbulent gas becomes indistinguishable from a subsonic turbulent gas.

Despite the clear gradient in initial clumping factor positively correlated with $\dot{\epsilon}_i$, the curves and error regions converge and reach C_{sub} on roughly the same timescales

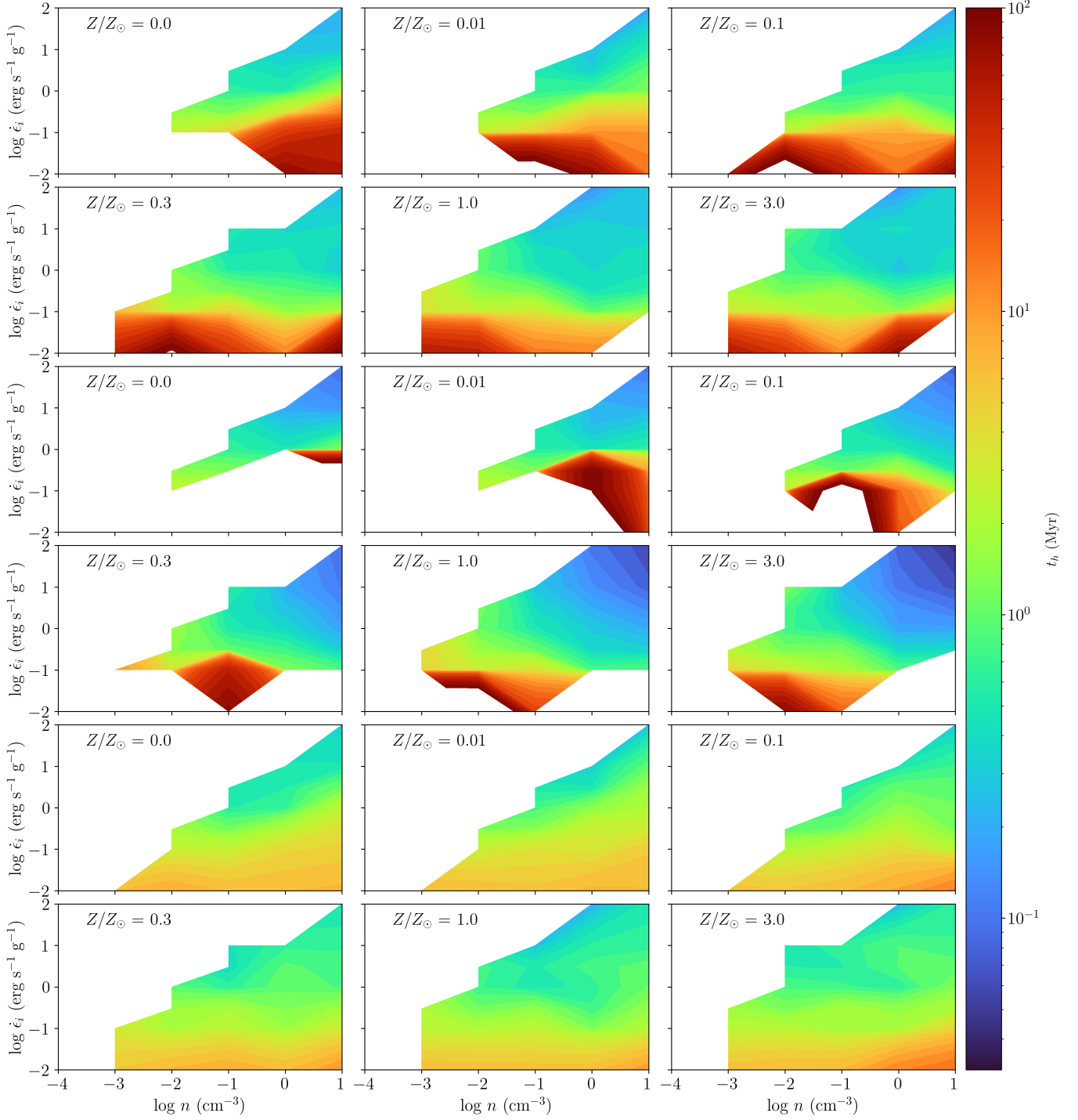


Figure 10. 2D contour maps of the half energy dissipation timescales t_h , defined as $\epsilon(t_h) = 0.5\epsilon_0$, across only supersonic runs. The blank regions on the top left above the diagonal represent subsonic runs, and the blank regions on the bottom represent supersonic runs which did not dissipate half the component of energy in question. The first and second rows shows total energy, the middle third and fourth rows show thermal energy, and the bottom fifth and sixth rows show kinetic energy

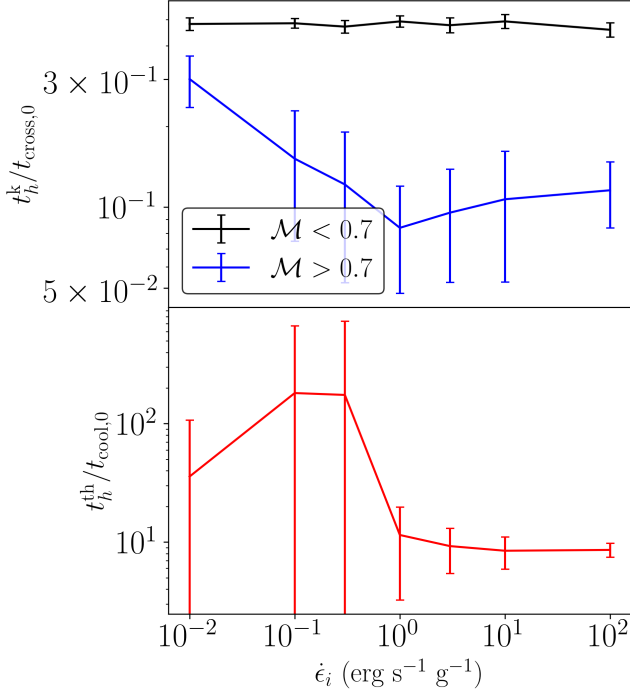


Figure 11. Dimensionless dissipation timescales t_h , defined as $\epsilon(t_h) = 0.5\epsilon_0$, for both kinetic (top) and thermal (bottom) energy as a function of ϵ_i . Kinetic energy is normalized by $t_{\text{cross},0}$ while thermal energy is normalized by $t_{\text{cool},0}$. Kinetic dissipation timescales are additionally separated between supersonic (blue) and subsonic (black) runs.

of around 100 Myr, albeit with some spread between 30 and 300 Myr. When binned in n on the bottom plot, a positive n dependence in t_{Diss}^C emerges. The shrinkage of the error regions encapsulates the same variations in ϵ_i converging in the top plot. Harkening back to Figures 5 and 7, dissipation in C is similar to but not congruent to dissipation in ϵ_k . While both quantities dissipates exponentially, kinetic energy dissipation does not depend on n .

We examine the intercorrelation between clumping factor dissipation and energy dissipation more closely in Figure 13. Since the locations of the squares denote a fixed time $t = 100$ Myr, the lower the position of the square, the shorter t_{Diss}^C is. We note that only the two lowest values of n are remotely representative of conditions in the CGM, and our purpose of showing $n = 1 \text{ cm}^{-3}$ and $n = 10 \text{ cm}^{-3}$ is to illustrate a trend. Given their similar dissipative behaviours in Figures 5 and 12, the middle plot unsurprisingly shows a steady power law relation between C and ϵ_k . The correlation with thermal dissipation in the top plot is much less smooth, and mirrors the the time tracks in Figure 6. C only shows a power law relation with ϵ_g during the rapid thermal dissipation epoch, continues to dissipate during

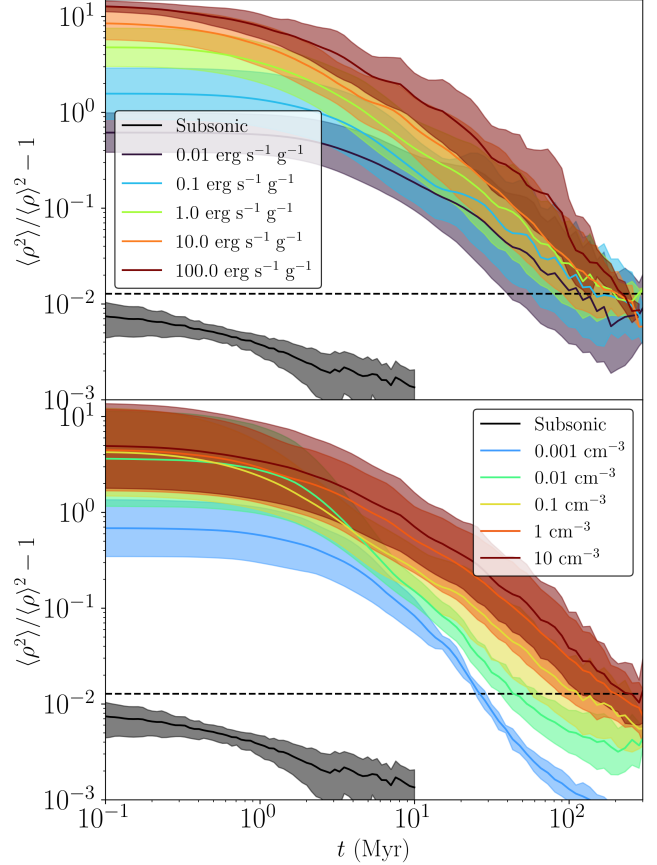


Figure 12. The dissipation of the clumping factor $\langle \rho^2 \rangle / \langle \rho \rangle^2 - 1$ over time. Consistent with previous plots, the coloured lines show various binnings in initial simulation parameters across supersonic runs. The black line and shaded region shows the average and 1σ across all subsonic runs, and the dotted line shows 5σ across all timesteps for all subsonic runs. *Top:* Clumping factor dissipation binned in ϵ_i . *Bottom:* Clumping factor dissipation binned in n

the ϵ_g plateau. There is a nonlinear relation between initial C and n , with $n = 0.01 \text{ cm}^{-3}$ and $n = 10 \text{ cm}^{-3}$ exhibiting higher clumping factors than the other runs. We again observe and affirm the negative correlation in the top plot between n and C at 100 Myr as seen in Figure 12, but we also note the dissipated steady state behaviour of ϵ_g . The more diffuse runs with lower clumping factors at 100 Myr have hotter thermal energy plateaus, with the $n = 0.01 \text{ cm}^{-3}$ and $n = 0.1 \text{ cm}^{-3}$ not even reaching the 1000 K temperature floor.

We affirm this trend holds statistically via an examination across all supersonic turbulent runs in Figure 14, and it becomes evident the n dependence of t_{Diss}^C represents a more fundamental positive dependance on $t_{\text{cool}}/t_{\text{cross}}$. The more inefficient the cooling, the more uniform the medium becomes. There are no discern-

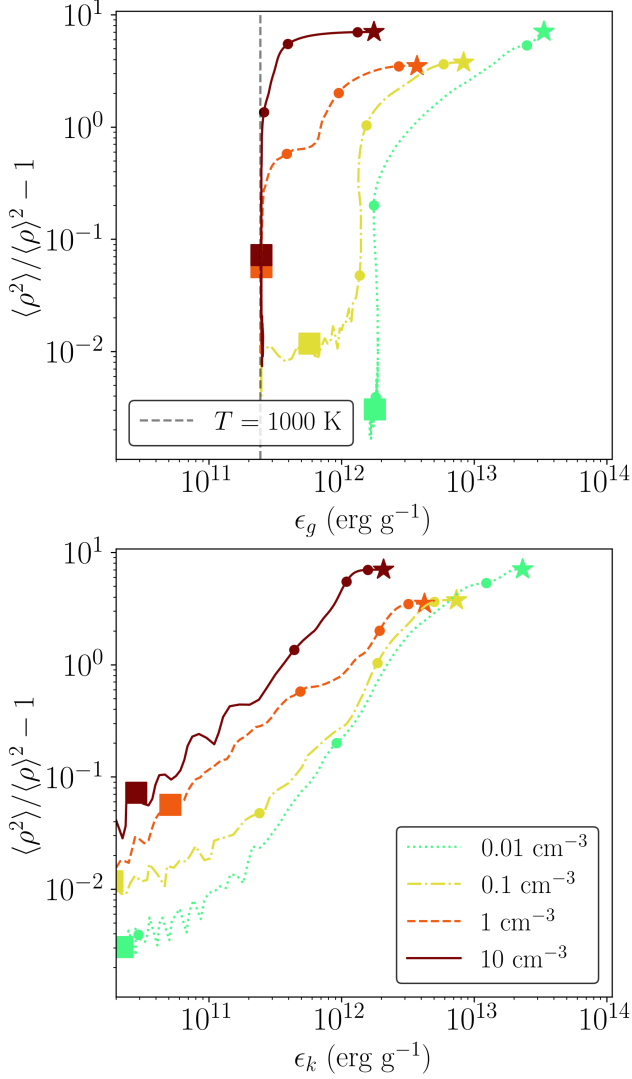


Figure 13. Phase plots tracking the temporal evolution of specific thermal (Top), specific kinetic energy (Bottom) relative to clumping factor. Four 128^3 resolution runs are shown, corresponding to $Z/Z_\odot = 0.3$, $\dot{\epsilon}_i = 1 \text{ erg s}^{-1} \text{ g}^{-1}$ and n ranging from 0.01 cm^{-3} to $n = 10 \text{ cm}^{-3}$. Similar to Figure 6, stars denote the turbulence driving turn off time where each curve begins, circular dots denote t_s , $10t_s$ and $100t_s$ as one moves from the star and along the curve, and squares denote the 100 Myr mark. The black dotted line in the top plot marks the $T = 1000 \text{ K}$ point.

able trends in the colouring of the data points, showing that neither $t_{\text{cool}}/t_{\text{cross}}$ nor t_{Diss}^C correlate significantly with the process of thermal dissipation. Rather, the dependence of t_{Diss}^C on $t_{\text{cool}}/t_{\text{cross}}$ reflects a dependence on the current dynamical state of the gas. Going back to Figure 13, despite having similar kinetic energies at 100 Myr, the $n = 0.01 \text{ cm}^{-3}$ run has distinctly more thermal energy than the $n = 10 \text{ cm}^{-3}$ run at that time, representing a smaller $t_{\text{cool}}/t_{\text{cross}}$ and hence a shorter density

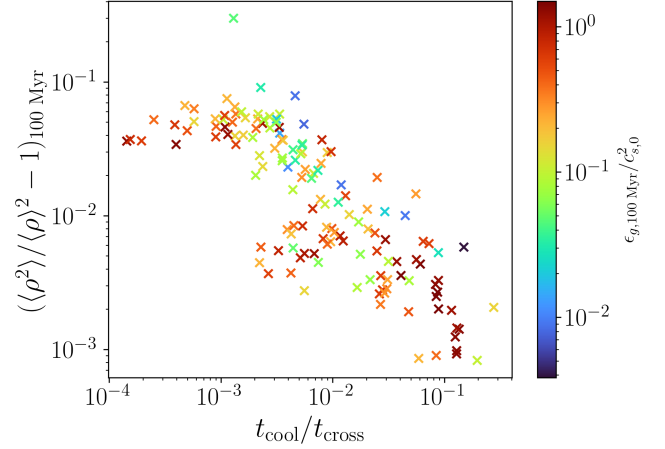


Figure 14. The ratio between t_{cool} and t_{cross} at turbulence turnoff versus the clumping factor $\langle \rho^2 \rangle / \langle \rho \rangle^2 - 1$ at 100 Myr. Each point represents a supersonic turbulent run, with the colour bar and marker colours denoting the normalized thermal energy $\epsilon_g/c_{s,0}^2$ at 100 Myr. As with previous figures, $c_{s,0}$ represents the sound speed at turbulence turnoff.

homogenization timescale, as the gas cannot cool fast enough to prevent the bulk motions from diffusing and smoothing out overdensities.

3.6. Fourier Analysis of Turbulent Clouds

In this section we characterize the turbulence driven overdensities and clouds in more detail. While C can broadly describe the overall "clumpiness" of the medium, it is insufficient in characterizing properties such as the spatial scales or \mathcal{M} of the substructures. We extend our power spectrum analysis from Figure 8 to more gas properties, following similar methods to those of Federrath & Klessen (2013). For some field $q(\vec{r})$ over \mathbb{R}^3 , its power spectrum is defined as

$$P_q(k) = k^2 \int d\Omega_k |\hat{q}(\vec{k})|^2 \quad (7)$$

where $\int d\Omega_k$ represents a solid angle integral over k -space, and k represents the radial component of \vec{k} . $\hat{q}(\vec{k})$ represents the Fourier Transform (FT) of the field q :

$$\hat{q}(\vec{k}) = \frac{1}{(2\pi)^3} \int q(\vec{r}) e^{-i\vec{k}\cdot\vec{r}} d^3r \quad (8)$$

Figure 15 paints a physical picture of the gas during steady state turbulence and during dissipation. While it's evident from Figure 12 there should be higher density contrasts with higher $\dot{\epsilon}_i$, another effect of stronger driving is a dramatic shrinking in the typical clump sizes. The $\dot{\epsilon}_i = 1 \text{ erg s}^{-1} \text{ g}^{-1}$ run sees clumps of order 10^2 pc , while the $\dot{\epsilon}_i = 10 \text{ erg s}^{-1} \text{ g}^{-1}$ run sees clumps of order 10^0 to 10^1 pc in size. There is a

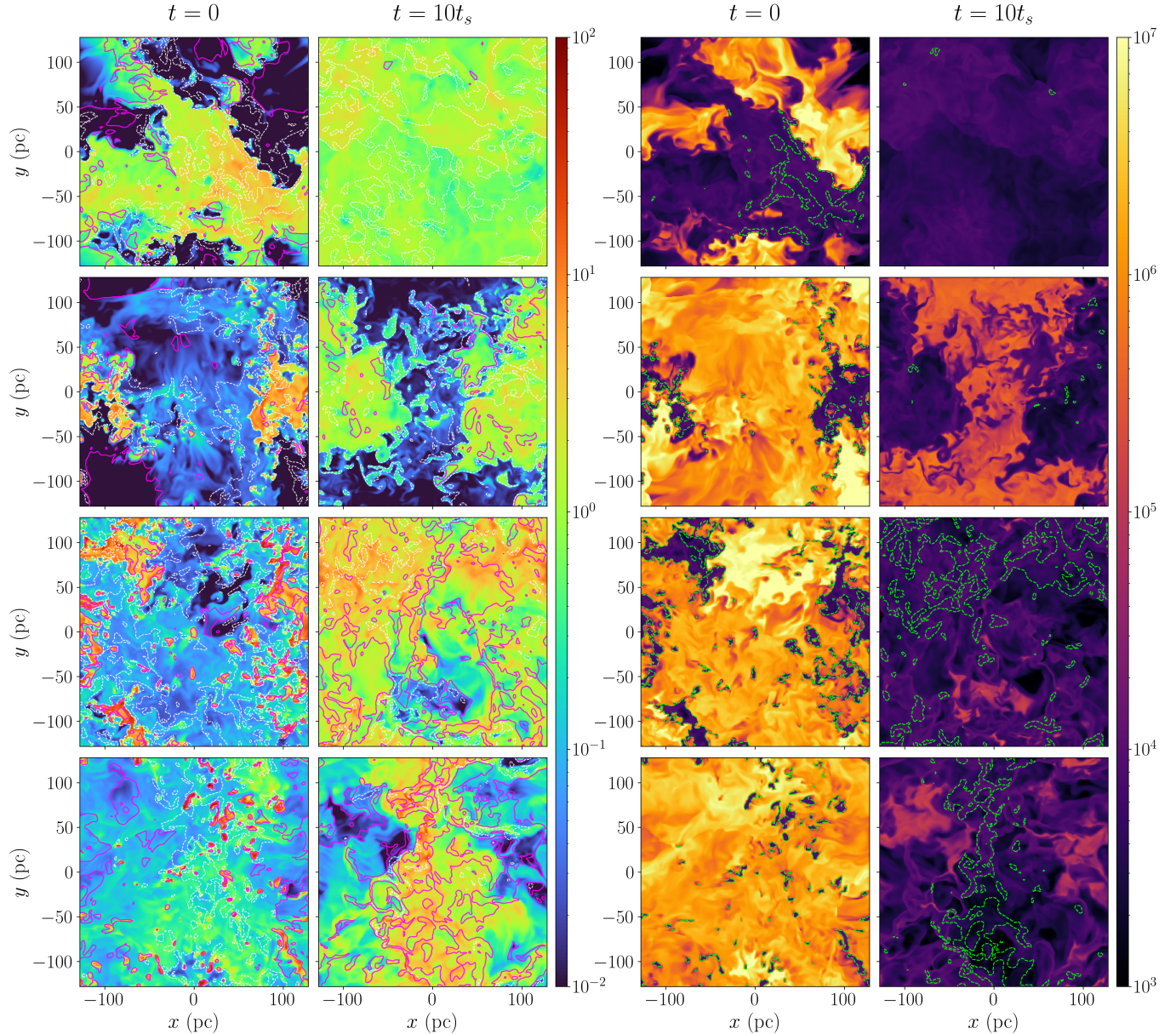


Figure 15. Density (Left) and temperature (Right) slice plots of four 256^3 resolution runs corresponding to $Z/Z_\odot = 0.3$, $n = 0.1 \text{ cm}^{-3}$. Each row corresponds to a different value of $\dot{\epsilon}_i$ - from top to bottom they are: $0.1 \text{ erg s}^{-1} \text{ g}^{-1}$, $1 \text{ erg s}^{-1} \text{ g}^{-1}$, $3 \text{ erg s}^{-1} \text{ g}^{-1}$ and $10 \text{ erg s}^{-1} \text{ g}^{-1}$. The densities and colour bar are normalized by the initial density $n = 0.1 \text{ cm}^{-3}$. The columns show the gas at different times, the first and third columns right at turbulence turnoff, the second and fourth columns at $10t_s$. On the density slice plots, dashed white lines show $\mathcal{M} = 1$ contours and solid magenta lines show $\mathcal{M} = 3$ contours. On the temperature slice plots, dashed lime lines show $\rho/m_p/n = 3$ contours .

nonlinear though clear inverse relation between driving strength and clump size. Weak turbulence driving, as seen in the $\dot{\epsilon}_i = 0.1 \text{ erg s}^{-1} \text{ g}^{-1}$ run, sees diffuse "bubbles" rather than dense clumps. The $\mathcal{M} = 1$ contours weakly trace the boundaries between diffuse and dense regions, and whose ubiquity shows both regions to be broadly supersonic. The $\mathcal{M} = 3$ contours show even more limited overlap with overdense regions in the top two plots, but trace dense regions very well in the

bottom two plots. Only under strong turbulence driving where $\dot{\epsilon}_i \geq 3 \text{ erg s}^{-1} \text{ g}^{-1}$ do we observe strongly supersonic clumps. In the temperature plots on the two left columns, the cool regions correlate very well with the dense regions on the two right columns, and share similar temperatures of 10^3 to 10^4 K across all four runs. This would suggest that faster bulk motions within the clumps is a significant contributor towards their increased compressibility.

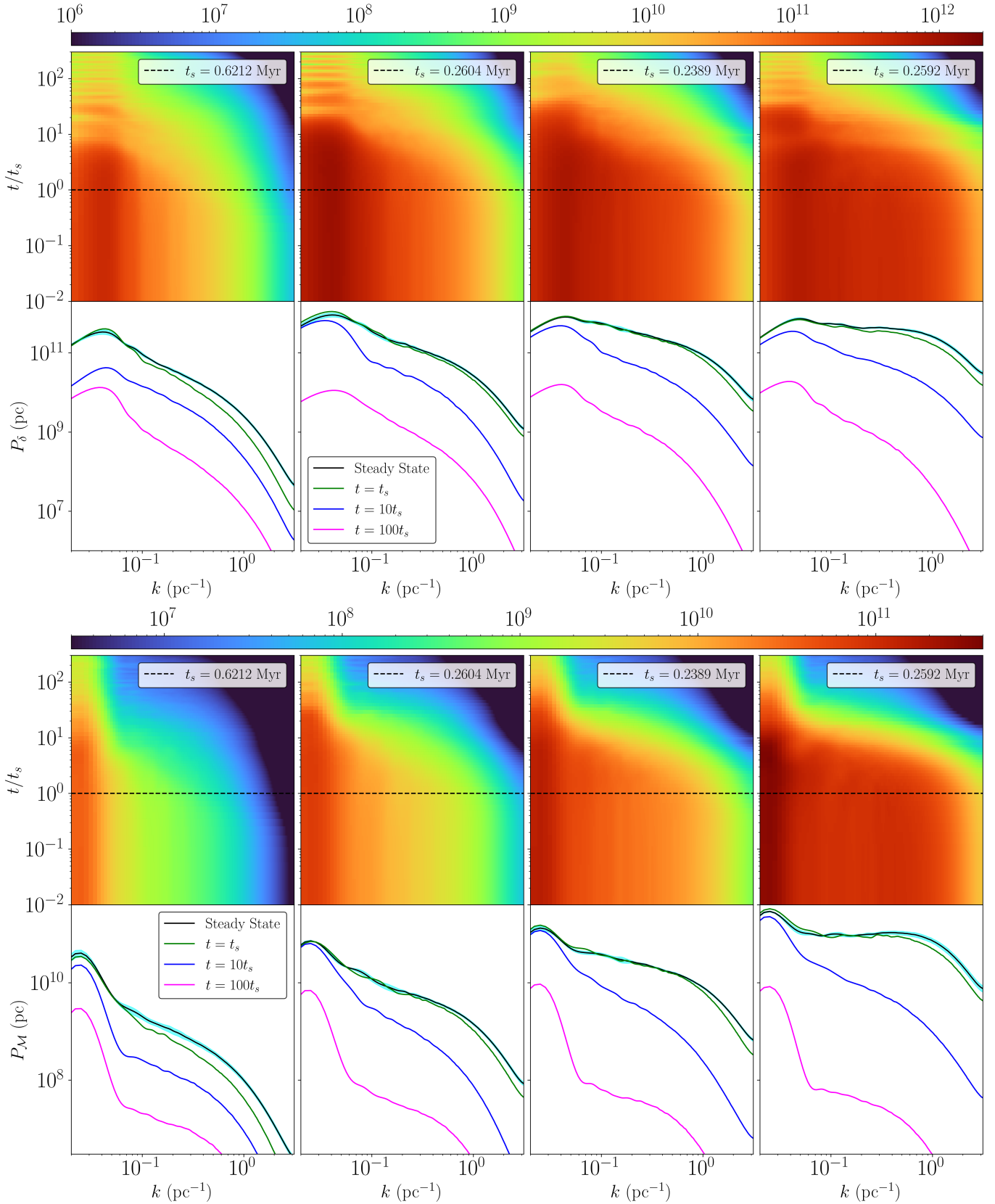


Figure 16. The density (Top) and \mathcal{M} (Bottom) power spectra of the four high resolution 256^3 runs shown in Figure 6, where $Z/Z_\odot = 0.3$ and $n = 0.1 \text{ cm}^{-3}$, and ϵ_k being 0.1, 1, 3.0 and 10.0 $\text{erg s}^{-1} \text{g}^{-1}$ from left to right. The bottom row plots the turbulence power spectra during steady state turbulence, after t_s , $10t_s$ and $100t_s$. The cyan coloured region represents 1σ across the last twenty outputs of the steady state turbulence epoch. The top row plots the power spectra from turbulence turn off up to $100t_s$, with the colour denoting ϵ_k . The value of t_s is also shown across each of the four runs. Both the top and bottom row plots are smoothed using degree-5 polynomial splines for visualization purposes.

We characterize the spatial scalings of \mathcal{M} via a power spectrum of the mach number. Following equations (7) and (8) we define $P_q(k) = P_{\mathcal{M}}(k)$ and $\hat{q}(\vec{k}) = \hat{\mathcal{M}}(\vec{k})$ from $q(\vec{r}) = \mathcal{M}(\vec{r})$, where $\mathcal{M}(\vec{r})$ represents the spatial mach number define as:

$$\mathcal{M}(\vec{r}) = \frac{|\vec{v}(\vec{r})|}{c_s(\vec{r})} \quad (9)$$

Similarly we can characterize the spatial scalings of the overdensities using the matter power spectrum $P_\delta(k)$, for which $q(\vec{r}) = \delta(\vec{r})$ where δ is a dimensionless overdensity parameter defined as

$$\delta(\vec{r}) = \frac{\rho(\vec{r}) - \bar{\rho}}{\bar{\rho}} \quad (10)$$

where $\bar{\rho}$ represents the spatially averaged density across the box, although functionally this equates to the initial density of the run.

In Figure 16, we characterize the dissipation of the dense clumps as seen in Figure 15 via the time evolution $P_{\mathcal{M}}$ and P_δ across the same four runs. Both power spectra exhibit broken $k^{-\alpha}$ power laws, with higher $\dot{\epsilon}_i$ corresponding to shallower α in the $0.07 < k < k_d$ range, where $k_d \approx 1 \text{ pc}^{-1}$ during turbulence driving. We will refer to this range in k as the linear range, the slope of the linear range as α_δ and $\alpha_{\mathcal{M}}$ for P_δ and $P_{\mathcal{M}}$ respectively, and $k > k_d$ as the dissipation range. The maxima of P_δ for $\dot{\epsilon}_i = 3 \text{ erg s}^{-1} \text{ g}^{-1}$ and $\dot{\epsilon}_i = 10 \text{ erg s}^{-1} \text{ g}^{-1}$ are around the same as if not lower than the maxima for $\dot{\epsilon}_i = 1 \text{ erg s}^{-1} \text{ g}^{-1}$, representing a larger proportion of the overdensities being captured at smaller scales. A shallow α_δ represents not just the presence of distinct clumps at small scales, but hierarchically structured clumping, where dense clumps host even denser clouds within. For $P_{\mathcal{M}}$, a shallower $\alpha_{\mathcal{M}}$ represents those same clumps being increasingly supersonic due to underpressurization from enhanced cooling. The rise in the linear range is also noticeably sharper from $\dot{\epsilon}_i = 3 \text{ erg s}^{-1} \text{ g}^{-1}$ to $\dot{\epsilon}_i = 10 \text{ erg s}^{-1} \text{ g}^{-1}$, which is consistent with Figure 15.

During dissipation, P_δ sees a steady increase in α_δ and decrease in k_d , which represents hierarchical dissipation of substructures beginning at the smallest scales. We see this in Figure 15 (primarily for $\dot{\epsilon}_i \geq 1 \text{ erg s}^{-1} \text{ g}^{-1}$), where at $10t_s$, the gas is smoother on smaller scales compared to how it is at t_s , while preserving its clumpiness on larger scales. $P_{\mathcal{M}}$ dissipates more irregularly, given its strong coupling with cooling rate Λ . While k_d also decreases, $\alpha_{\mathcal{M}}$ evolves very differently when compared with α_δ . For $\dot{\epsilon}_i = 0.1 \text{ erg s}^{-1} \text{ g}^{-1}$, there is no significant change in $\alpha_{\mathcal{M}}$, while for the three runs with higher $\dot{\epsilon}_i$, $\alpha_{\mathcal{M}}$ increases between $t = 0$ and $t = 10t_s$ and decreases between $t = 10t_s$ and $t = 100t_s$. The drop in

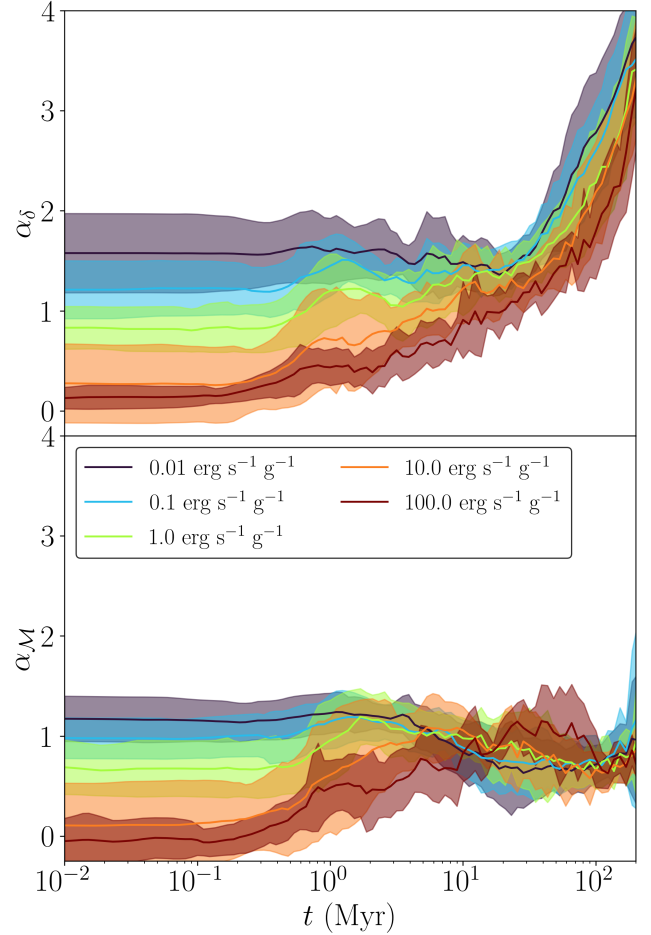


Figure 17. The power law indices of $P_{\mathcal{M}}$ (Top) and P_δ (Bottom) over time across supersonic 128^3 runs. The linear range power laws are separated in $\dot{\epsilon}_i$, and the dissipation range power laws are coagulated and shown in black. The shaded regions represent 1σ .

amplitude is more significant than that of P_δ and scales with increasing k , where cooling becomes increasingly dominant.

The shortened cloud survival timescales at efficient cooling regimes does not contradict existing evidence that radiative cooling supports cloud (Gronke & Oh 2018, 2020; Li et al. 2020). Rather, it speaks on the typical sizes of such clouds. The dissipation of clouds due to shockwaves is governed by cloud-crushing timescale (Klein et al. 1994) defined as

$$t_{\text{cc}} = \frac{\chi^{1/2} a_0}{v_b} \quad (11)$$

where χ is the dimensionless cloud overdensity factor, a_0 the cloud radius and v_b the incoming shock velocity. Clouds can only survive shocks when $t_{\text{cool}} < t_{\text{cc}}$ (Cooper et al. 2009; Gronke & Oh 2018, 2020), when a significant pressure gradient can be maintained between the cloud

and the intracloud medium. The destruction of clouds as seen in the steepening of α_δ and the difference between the $t = 0$ and $t = 10t_s$ snapshots in Figure 15 show that $t_{\text{cool}} > t_{\text{cc}}$ on all scales. Assuming a uniform "intracloud medium" shock speed v_b when integrated across all clouds in all directions given our uniform randomized turbulence driving scheme (See Section 2), the typical cloud size must then have a sharp inverse dependence on χ , where $a_0 \propto \chi^{-\beta}$ for $\beta > 3/2$ since $t_{\text{cool}} \propto \chi^{-2}$. We note this as a generalized empirical result given the non-ideal conditions of our simulations and our broader focus on global energy and substructure dissipation, whereas detailed studies on cloud survival and crushing employ idealized wind tunnel simulations (Klein et al. 1994; Xu & Stone 1995; Cooper et al. 2009; Gronke & Oh 2018, 2020; Li et al. 2020; Kanjilal et al. 2021).

We compute $\alpha_{\mathcal{M}}$ and α_δ via a curve fit using the Levenberg-Marquardt least-squares algorithm (Marquardt 1963) for $0.07 < k < k_d$. To account for the shrinking of k_d over time, multiple curve fits are performed for each run at each timestep for $0.2 < k_d\pi/4$, and the fit with the smallest error is chosen. The bounds are chosen from visual inspection of the 128^3 resolution power spectra, encapsulating the full range of k_d across all runs and all times.

We show the power indices for $P_{\mathcal{M}}$ and P_δ over time across all our supersonic 128^3 runs in Figure 17. Both power spectra show an initial gradient in α , with higher $\dot{\epsilon}_i$ leading to shallower α . The power law indices for P_δ in the top plot initially converge up until 10 Myr, beyond which they begin to sharply steepen. Meanwhile for $P_{\mathcal{M}}$, the power law indices also initially converge up until the same time, but remain more or less unchanged as a whole beyond that time, with $\dot{\epsilon}_i = 100 \text{ erg s}^{-1} \text{ g}^{-1}$ serving as a mild outlier. Both behaviours are consistent with Figure 16. As with C in Figure 12, α shows distinct and synchronous trends with respect to absolute time t , but unlike Figure 12, this no distinct n dependence in the time evolution of α . The steepening of α in the top plot represents the crushing of small scale clouds, and from the convergent behaviour of the curves we see that similar to t_{Diss}^C , the cloud crushing timescales are weakly coupled to if not independent from $\dot{\epsilon}_i$. Similar to Figure 12, we can roughly define a universal cloud crushing timescale t_{cc} to be approximately 10 Myr, representing the convergence point in the power law indices across all supersonic runs.

In Figure 18 we compare the time evolution of α in relation to the other quantities examined in this study, namely thermal energy, kinetic energy, and clumping factor. The initial state is broadly weakly supersonic where $\epsilon_g/\epsilon_k \approx 1$ with the clumps being strongly super-

sonic as seen from Figure 15. C and ϵ_k are more or less parallel, affirming our earlier observations and discussions. The bulk of the dissipation occurs between t_s and $10t_s$, where a sharp drop in ϵ_g corresponds to a steepening in $\alpha_{\mathcal{M}}$ and α_δ . For a brief period of time between $3t_s$ and $20t_s$, the gas is strongly supersonic due to rapid thermal cooling, and within this period we observe C , $\alpha_{\mathcal{M}}$ and α_δ to roughly flatten out at various points. This may be indicative of temporary stabilization against cloud collapse, where the clouds become significantly larger and colder resulting in longer t_{cc} and stronger pressure gradients between the cloud and intracloud medium.

4. DISCUSSION

4.1. On the Nature of Supersonic Thermal and Kinetic Dissipation

Thermal and kinetic energy exhibit vastly different dissipative behaviours. The bulk of the thermal energy dissipates during the initial rapid dissipation epoch while kinetic energy maintains a consistent exponentially decaying rate. The physics behind the rapid thermal dissipation epoch results from enhanced cooling in dense clouds, evidenced by stronger turbulence driving leading to a clumpier medium, shallower P_δ power law and increased thermal dissipation as seen in Figures 12, 16 and 5. Thermal dissipation is then strongly coupled to turbulence driving indirectly through increased clumping. Kinetic dissipation on the other hand occurs via energy cascade into thermal energy, per the following relation in the inertial regime as derived by Kolmogorov (1941):

$$E_k = C_k k^{-5/3} \dot{\epsilon}_k^{2/3} \quad (12)$$

As seen in Figure 8, our simulations follow the $k^{-5/3}$ power law quite well, despite the bottleneck effect (Dobler et al. 2003). We note that since we cannot resolve the kolmogorov microscales and we did not introduce additional subgrid artificial viscosity, the cascade occurs via only shock heating and numerical dissipation, which may have represented an underestimation of up to 50% (Stone et al. 1998). In comparatively stronger supersonic regimes, the power law approaches k^{-2} for a fully shocked gas (Burgers 1948) and the bottleneck effect becomes less significant (Federrath et al. 2010; Federrath & Klessen 2013). While we do achieve strongly supersonic regions within dense clumps, overall our supersonic runs are weakly supersonic where \mathcal{M} and ϵ_k/ϵ_g are of order unity during steady state turbulence, due to shock heating of the gas and inefficient cooling regimes beyond the local maximum along Λ beyond 10^4 to 10^5 K depending on Z/Z_\odot . This kinetic dissipation rate

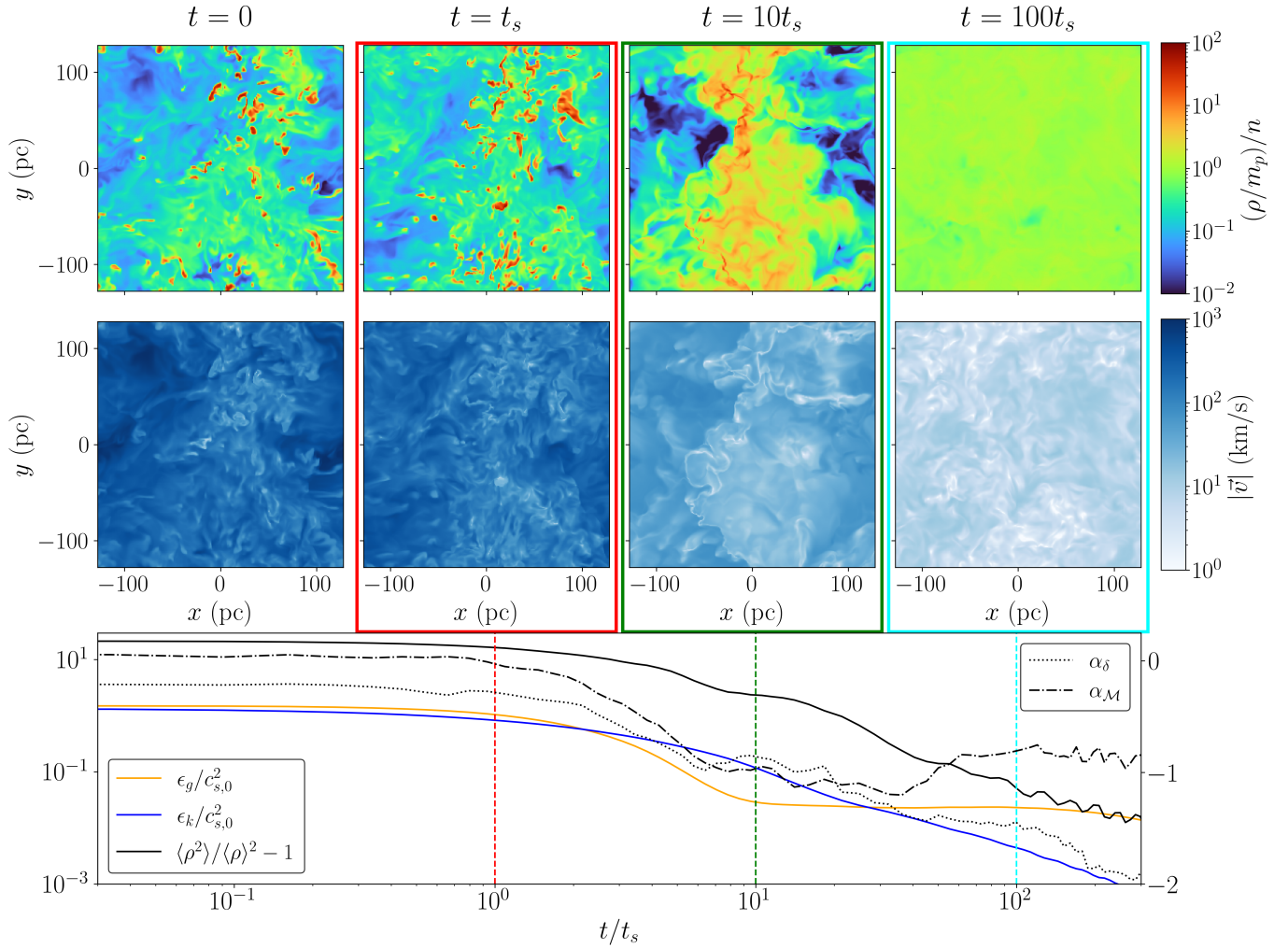


Figure 18. The full set of dissipation curves for the $Z/Z_\odot = 0.3$, $n = 0.1 \text{ cm}^{-3}$, and $\dot{\epsilon}_i = 10 \text{ erg s}^{-1} \text{ g}^{-1}$. Across four distinct snapshots $t = 0, t_s, 10t_s, 100t_s$, the top row plots density slices normalized by n while the middle row plots velocity magnitude. The bottom plot shows five dimensionless dissipation curves over time normalized by t_s : thermal energy ($\epsilon_g/c_{s,0}^2$), kinetic energy ($\epsilon_k/c_{s,0}^2$), clumping factor ($C = \langle \rho^2 \rangle / \langle \rho \rangle^2 - 1$), matter power spectrum linear regime power index (α_δ) and mach power spectrum linear regime power index (α_M). The former three quantities are shown on the left y axis, while the latter two are shown on the right y axis. The red, green and cyan dotted lines on the bottom plot corresponding to the boxes of the same colour around the slice plots show the times slice plots represent.

$\dot{\epsilon}_k^{2/3}$ depends only on E_k , which leads to an indirect coupling with $\dot{\epsilon}_i$ where strong turbulence driving leads to higher initial kinetic energy. However this correlation only results in exponential dissipation, which leads to convergence in the kinetic energy curves across all turbulence driving strengths. We observe similarities with Stone et al. (1998) and Ostriker et al. (1999) with the shapes of our kinetic dissipation curves, although in our case it takes up to $100t_s$ for kinetic energy to dissipate by 1 dex, while in their case 1 dex dissipation occurs within $0.1t_s$. Substructures, as the product of shock compression during turbulence driving, naturally couple with kinetic energy and dissipate similarly. Their lifetimes and dissipation rate are also coupled with thermal

dissipation, since strong cooling and further underpressurization within the cloud leads to increased cloud stability against crushing (Cooper et al. 2009; Gronke & Oh 2018, 2020).

4.2. On the Formation and Crushing of Turbulent Clouds

In circumgalactic environments stable against Jeans collapse, turbulence and radiative cooling become the primary drivers of turbulent cloud formation. Turbulence drives density fluctuations in the medium, which in turn overcool and trigger condensation (Mo & Miralda-Escude 1996; Maller & Bullock 2004; Armillotta et al. 2016; Chen et al. 2023), forming dense clouds. For strong turbulence driving we observe this to be hier-

archical, with further condensation and denser clumps forming within existing overdensities. Such clouds remain stable via a strong pressure gradient between regions internal and external to the cloud, where the hot high pressure external region spatially confines the cool low pressure cloud (Li et al. 2020). Turbulence driving maintains the strong pressure gradient, where kinetic energy is continuously, uniformly and isotropically injected into our box, which cascades into thermal energy and heats the medium. Dense clouds remain cool at around 10^4 K since they can efficiently thermally dissipate the additional energy, but the diffuse medium must climb to higher temperatures of $10^5 - 10^6$ K, where Λ reaches its local maxima depending on Z/Z_\odot , in order to reach thermal equilibrium with turbulence driving (the run becomes subsonic if thermal equilibrium cannot be reached at those local maxima). Gronke & Oh (2018, 2020) showed that stable clouds can grow via entraining and mixing with hot gas on its boundary layers. However, those findings are based in idealized wind tunnel simulations, and we cannot confirm whether this is present in our simulations since our "winds" are effectively isotropic.

Our clouds are eventually "crushed" via cooling of the intracloud medium, which is consistent with Li et al. (2020). From Figure 15, the diffuse gas cools significantly after $10t_s$ for the $\dot{\epsilon}_i = 10 \text{ erg s}^{-1} \text{ g}^{-1}$, representing the end of the rapid thermal dissipation epoch as seen in Figure 18. Figures 12 and 17 show trends only with respect to t as opposed to dimensionless time such as t/t_s . The n dependence arises from enhanced cooling stabilizing clouds against dissipation, although it is only present for t_{Diss}^C and absent for t_{cc} . The independence of both timescales from $\dot{\epsilon}_i$ raises interesting questions on the interdependencies between χ , a_0 and v_b in eq. (11). From visual inspection, $\dot{\epsilon}_i$ shares an inverse relation with a_0 , but a positive relation with v_b and χ , which may end up constraining t_{cc} . A future study focused on the formation and dissipation of turbulence driven clouds, particularly in non-idealized environments such as ours, is highly warranted.

4.3. Physical Implications of the Density Homogenization and Cloud Crushing Timescales

The density homogenization timescales of 30 – 300 Myr and cloud crushing timescales of 10 Myr independent of turbulence driving strength may have multiple physical implications. On the brevity of such timescales, warm and cool clouds are ubiquitously observed in the CGM (Stocke et al. 2013), while the dynamical time on circumgalactic scales is several hundred Myr (Heckman et al. 1991) and freefall time up to a Gyr, several

times longer than the structural dissipation timescales. While we neglected microphysics such as conduction which may play an important role in cloud stabilization ((Braginskii 1965; Li et al. 2020), a more likely explanation would be periodic feedback-driven outflows from the galactic disc ((Rubin et al. 2014; Nielsen et al. 2015; Borthakur et al. 2013) with hot outflow gas accelerating and shocking the cool CGM gas (Thompson et al. 2016), though Muratov et al. (2015) found galactic outflows to be bursty with periods of up to hundreds of Myr in the FIRE simulations (Hopkins et al. 2014). On the other hand, feedback from galactic nuclear regions occur on much shorter timescales of 10s of Myr, particularly for barred galaxies (Krumholz & Kruijssen 2015), from which the feedback of nuclear star clusters are capable of forming massive biconical outflows (Tenorio-Tagle & Muñoz-Tuñón 1998; Tenorio-Tagle et al. 2005; Schneider et al. 2020). A possible alternate or compounding explanation is that haloes exhibiting such clouds are unvirialized and hence see turbulence driven by supersonic cold streams (Stern et al. 2021). On the independence of such timescales relative to $\dot{\epsilon}_i$ may also serve as a method of ascertaining when the last perturbation occurred regardless of driving strength, from starburst/AGN driven outflows to accretion flows. However, the positive n dependence of the density homogenization timescales would require a proper spatial characterization of CGM densities, which is a challenging task given the complex multiphased nature of the CGM (Tumlinson et al. 2017).

4.4. Future Work

While the non self-gravitating and optically-thin approximations are valid for our diffuse runs, they become less accurate for our denser runs of $n \geq 1 \text{ cm}^{-3}$ where our conditions begin to approach those of the ISM. More detailed exploration of these denser phases, with consistent thermochemistry and self-gravity, would serve as a bridge between our study and existing studies on turbulence dissipation in GMCs. Additionally, while magnetic fields are secondary to radiative cooling in stabilizing clouds against crushing, they play an important role in GMCs. We would recommend the inclusion of magnetic fields in subsequent studies of these denser phases, or even subsequent studies of the diffuse phases for the sake of completion.

The highly nonlinear thermal dissipative behaviours highlight the impact of kinematics, compression and overdense clouds on thermal dissipation. Our energy dissipation timescales and curves can be applied in larger scale cosmological simulations in lieu of conventional cooling curves, where those overdense clouds we observe in this study cannot be explicitly resolved.

5. CONCLUSION

This work explores the saturation and dissipation of hydrodynamic turbulence with a large array of 252 simulations, covering and extending beyond the typical range of physical parameters describing typical conditions within the CGM. The conclusions are summarized as follows.

1. Energy dissipation from uniformly driven turbulence can be characterized into subsonic and supersonic categories depending on the compressibility of the gas. Supersonic dissipation sees an initial rapid epoch of thermal-dominated dissipation followed by a slower epoch of energy dissipation, while subsonic dissipation only sees slow dissipation. Thermal dissipation occurs rapidly within a few kinetic saturation times before plateauing, while kinetic dissipation follows a consistent exponential curve.
2. Thermal dissipation occurs via enhanced cooling, with a highly nonlinear but strongly positive correlation with turbulence driving strength which creates overdense clouds via shocks. Kinetic dissipation occurs via the energy cascade, and positively but more weakly couples to turbulence driving strength which increases the initial kinetic energy.

3. Substructure formation is observed in supersonic runs, with clumping factors ranging from 2 – 10 depending on turbulent driving strength and the density field spanning a few orders of magnitude. Subsonic turbulence sees mostly uniform gas, with clumping factor within 10^{-3} of 1 and the density field spanning less than single order of magnitude. The density homogenization timescale t_{Diss}^C , defined to be how long it takes for a supersonic run to become indistinguishable from a subsonic run, falls within the same order of magnitude across all runs at around 30 – 300 Myr depending on initial density but independent of turbulence driving strength.
4. Stronger turbulence driving yields denser, more concentrated and more compressible clouds, with flattened matter and \mathcal{M} power spectra in the linear range. Cloud crushing timescales, defined using the power indices of the power spectra, are 10 Myr regardless of turbulence driving, and unlike density homogenization timescales, are independent from n .

- 1 This work was supported by the National Science Founda-
 2 tion of China (11991052, 12233001), the National
 3 Key R&D Program of China (2022YFF0503401), the
 4 China Manned Space Project (CMS-CSST-2021-A04,
 5 CMS-CSST-2021-A06), and the Zhejiang Laboratory
 6 (K2022PE0AB01). Renyue Cen is supported in part by
 7 the National Key Research and Development Program
 8 of China.

APPENDIX

A. RESOLUTION DEPENDANCE

A.1. Energy Dissipation

We compare the dissipation curves between our high resolution runs and their low resolution counterparts in Figure 19. The lower resolution runs show slightly different initial energies with variations on order unity between 0.8 and 1.5 times the initial thermal and kinetic energies of the high resolution runs. The resolution difference manifests itself primarily as slight differences in the turbulent steady state, with the dissipation curves themselves showing near congruent behaviours. Qualitatively there is good resolution convergence. However, quantitative differences in the initial states leads to noticeable (and in some cases significant) quantitative differences in the dissipation timescales as seen in Table 1. The largest disparity can be seen in the thermal energy

dissipation timescales, where for $\epsilon_i = 0.1$ ($\text{erg s}^{-1} \text{g}^{-1}$) t_h varies by more than a factor of two. This is the result of the temperature dependence of the cooling curve, particularly at temperatures around 10^4 K where $\frac{d\Lambda}{dT}$ is particularly steep. Disparities in the kinetic dissipation timescales are less significant, and may result from the finer resolution scales underestimating the energy cascading rate due to our lack of subgrid viscosity. Increased resolution leads both to an increase or decrease in initial energies depending on driving strength, which suggests that resolution has a highly nonlinear effect on the initial conditions.

As a comparison, Stone et al. (1998) saw variations in total (kinetic + magnetic) energy of around 6% between their 128³ runs and their 256³ runs, which is significantly less than our variations of up to 50% in kinetic energy.

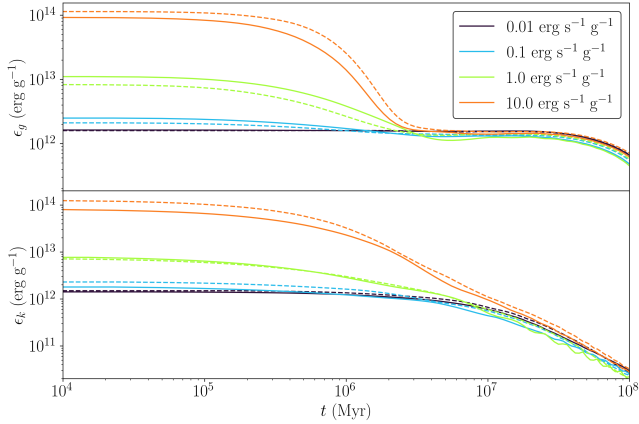


Figure 19. Thermal and kinetic dissipation curves comparisons between the fiducial high resolution 256^3 runs (solid line) and lower resolution 128^3 counterparts (dashed line). $Z/Z_\odot = 0.3$ and $n = 0.1 \text{ cm}^{-3}$ for these runs.

| $\dot{\epsilon}_i$ (erg s $^{-1}$ g $^{-1}$) | $128^3 t_h$ (Myr) | $256^3 t_h$ (Myr) |
|---|-------------------|-------------------|
| Total Energy | | |
| 0.01 | 36.0 | 37.4 |
| 0.1 | 4.71 | 3.74 |
| 1 | 0.548 | 0.563 |
| 10 | 0.524 | 0.431 |
| Thermal Energy | | |
| 0.01 | 87.5 | 84.8 |
| 0.1 | 51.0 | 23.9 |
| 1 | 0.510 | 0.599 |
| 10 | 0.592 | 0.432 |
| Kinetic Energy | | |
| 0.01 | 8.25 | 7.64 |
| 0.1 | 2.49 | 3.24 |
| 1 | 0.623 | 0.502 |
| 10 | 0.434 | 0.425 |

Table 1. Comparisons between half energy dissipation timescales t_h between the fiducial high resolution 256^3 runs and their respective lower resolution 128^3 counterparts.

This highlights the additional resolution sensitivity that emerges from an adiabatic equation of state, where kinetic energy is dissipated via the energy cascade as opposed to artificial numerical viscosity as implemented in ZEUS (Stone & Norman 1992b), which is the code used by Stone et al. (1998). We emphasize however that there is resolution convergence on the qualitative conclusions we make on the dissipation curves.

A.2. Power Spectra

We present the resolution comparisons of the power spectra in Figure 20. The 128^3 runs are shifted down by approximately 2 dex and have smaller k_d compared to the 256^3 runs. However, we did not utilize or consider the absolute amplitudes of the power spectra in our analysis, and k_d was determined dynamically through a series of curve fits for each run at each snapshot when fitting $\alpha_{\mathcal{M}}$ and α_δ . Beyond these differences, the shapes and trends are broadly consistent, with both P_δ and $P_{\mathcal{M}}$ for both resolutions seeing a flatter linear range with higher $\dot{\epsilon}_i$.

The bottleneck effect, which describes the accumulation of energy at high k in the inertial regime of the turbulence power spectrum, sees a dependence on both the compressibility of the gas (\mathcal{M}) as well as the resolution, being particularly relevant for higher resolution and strongly supersonic simulations (Dobler et al. 2003; Haugen et al. 2004; Federrath et al. 2010). We find that the bottleneck effect remains visible for both 128^3 and 256^3 runs, though strong compressibility does dampen it for the 128^3 resolution run in the bottom left plot.

REFERENCES

- Armillotta, L., Fraternali, F., & Marinacci, F. 2016, MNRAS, 462, 4157, doi: [10.1093/mnras/stw1930](https://doi.org/10.1093/mnras/stw1930)
- Balbus, S. A., & Soker, N. 1989, ApJ, 341, 611, doi: [10.1086/167521](https://doi.org/10.1086/167521)
- Bavassano, B., Dobrowolny, M., Mariani, F., & Ness, N. F. 1982, J. Geophys. Res., 87, 3617, doi: [10.1029/JA087iA05p03617](https://doi.org/10.1029/JA087iA05p03617)
- Borthakur, S., Heckman, T., Strickland, D., Wild, V., & Schiminovich, D. 2013, ApJ, 768, 18, doi: [10.1088/0004-637X/768/1/18](https://doi.org/10.1088/0004-637X/768/1/18)
- Braginskii, S. I. 1965, Reviews of Plasma Physics, 1, 205
- Burgers, J. M. 1948, Advances in Applied Mechanics, 1, 171. <https://api.semanticscholar.org/CorpusID:117400324>
- Burkhart, B., Collins, D. C., & Lazarian, A. 2015, ApJ, 808, 48, doi: [10.1088/0004-637X/808/1/48](https://doi.org/10.1088/0004-637X/808/1/48)

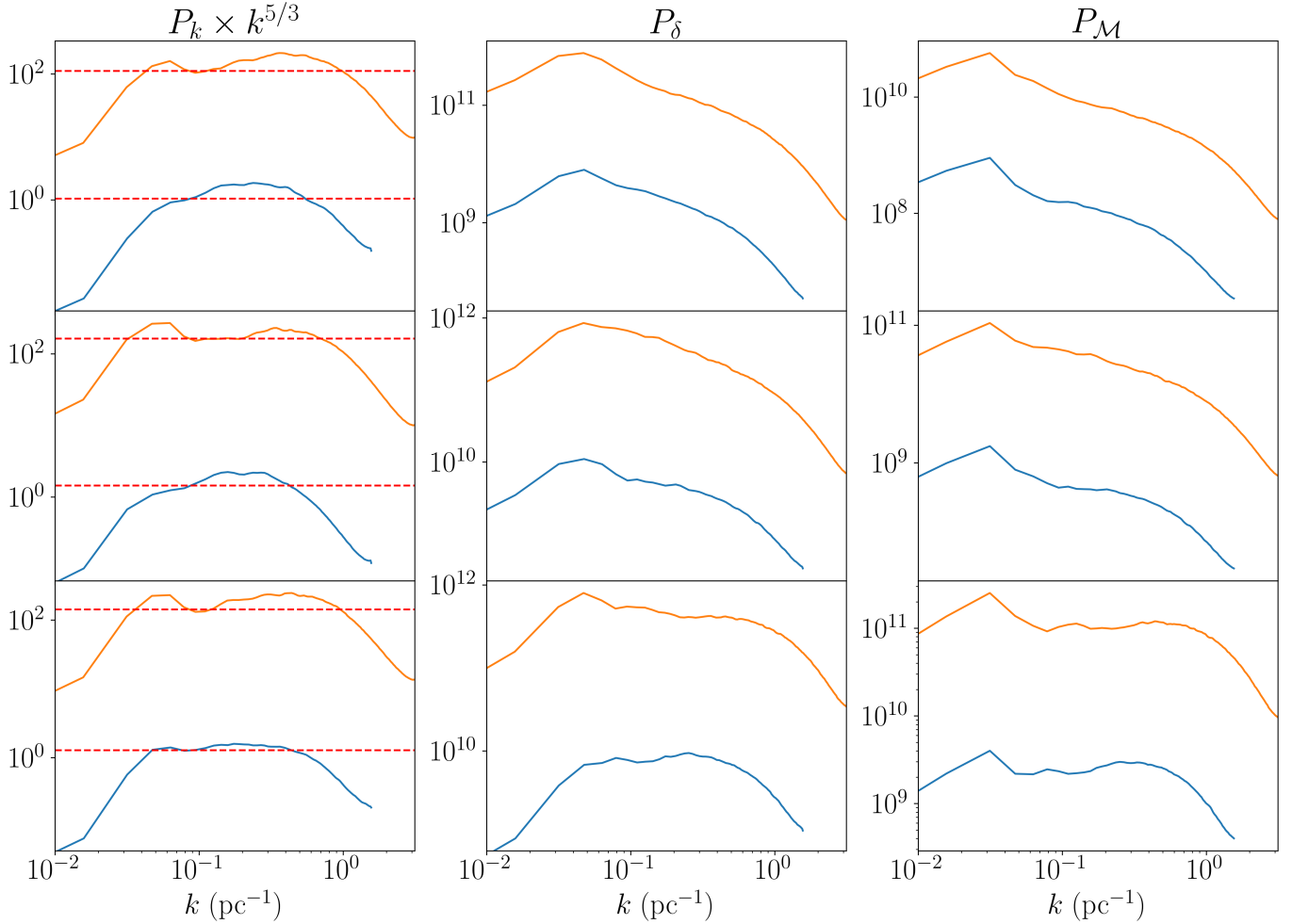


Figure 20. Comparisons between the power spectra of 128^3 (blue) and 256^3 (orange) resolution runs. From left to right we show the turbulence (P_k), matter (P_δ), and mach (P_M) power spectra. P_k is multiplied by the $k^{5/3}$ such that kolmogorov power law (red dotted) is a horizontal line. From top to bottom we have $\dot{\epsilon}_i = 1, 3$ and $10 \text{ erg s}^{-1} \text{ g}^{-1}$.

Bustard, C., & Oh, S. P. 2023, ApJ, 955, 64,

doi: [10.3847/1538-4357/aceef9](https://doi.org/10.3847/1538-4357/aceef9)

Cen, R. 2013, ApJ, 770, 139,

doi: [10.1088/0004-637X/770/2/139](https://doi.org/10.1088/0004-637X/770/2/139)

Chen, H.-W., Qu, Z., Rauch, M., et al. 2023, ApJL, 955,

L25, doi: [10.3847/2041-8213/acf85b](https://doi.org/10.3847/2041-8213/acf85b)

Cooper, J. L., Bicknell, G. V., Sutherland, R. S., &

Bland-Hawthorn, J. 2009, ApJ, 703, 330,

doi: [10.1088/0004-637X/703/1/330](https://doi.org/10.1088/0004-637X/703/1/330)

Crighton, N. H. M., Hennawi, J. F., & Prochaska, J. X.

2013, ApJL, 776, L18, doi: [10.1088/2041-8205/776/2/L18](https://doi.org/10.1088/2041-8205/776/2/L18)

Crighton, N. H. M., Hennawi, J. F., Simcoe, R. A., et al.

2015, MNRAS, 446, 18, doi: [10.1093/mnras/stu2088](https://doi.org/10.1093/mnras/stu2088)

Dekel, A., Sari, R., & Ceverino, D. 2009, ApJ, 703, 785,

doi: [10.1088/0004-637X/703/1/785](https://doi.org/10.1088/0004-637X/703/1/785)

Dobler, W., Haugen, N. E. L., Yousef, T. A., &

Brandenburg, A. 2003, Phys. Rev. E, 68, 026304,

doi: [10.1103/PhysRevE.68.026304](https://doi.org/10.1103/PhysRevE.68.026304)

Donzis, D. A., & Sreenivasan, K. R. 2010, Journal of Fluid

Mechanics, 657, 171, doi: [10.1017/S0022112010001400](https://doi.org/10.1017/S0022112010001400)

Faucher-Giguère, C.-A., & Oh, S. P. 2023, ARA&A, 61,

131, doi: [10.1146/annurev-astro-052920-125203](https://doi.org/10.1146/annurev-astro-052920-125203)

Federrath, C., & Klessen, R. S. 2013, ApJ, 763, 51,

doi: [10.1088/0004-637X/763/1/51](https://doi.org/10.1088/0004-637X/763/1/51)

Federrath, C., Roman-Duval, J., Klessen, R. S., Schmidt,

W., & Mac Low, M. M. 2010, A&A, 512, A81,

doi: [10.1051/0004-6361/200912437](https://doi.org/10.1051/0004-6361/200912437)

Fielding, D., Quataert, E., McCourt, M., & Thompson,

T. A. 2017, MNRAS, 466, 3810,

doi: [10.1093/mnras/stw3326](https://doi.org/10.1093/mnras/stw3326)

Gaspari, M., Ruszkowski, M., & Oh, S. P. 2013, MNRAS,

432, 3401, doi: [10.1093/mnras/stt692](https://doi.org/10.1093/mnras/stt692)

Gnedin, N. Y., & Hollon, N. 2012, ApJS, 202, 13,

doi: [10.1088/0067-0049/202/2/13](https://doi.org/10.1088/0067-0049/202/2/13)

Gronke, M., & Oh, S. P. 2018, MNRAS, 480, L111,

doi: [10.1093/mnrasl/sly131](https://doi.org/10.1093/mnrasl/sly131)

- . 2020, MNRAS, 492, 1970, doi: [10.1093/mnras/stz3332](https://doi.org/10.1093/mnras/stz3332)
- Gronke, M., Oh, S. P., Ji, S., & Norman, C. 2022, MNRAS, 511, 859, doi: [10.1093/mnras/stab3351](https://doi.org/10.1093/mnras/stab3351)
- Haugen, N. E. L., Brandenburg, A., & Dobler, W. 2004, Phys. Rev. E, 70, 016308, doi: [10.1103/PhysRevE.70.016308](https://doi.org/10.1103/PhysRevE.70.016308)
- Heckman, T. M., Lehnert, M. D., van Breugel, W., & Miley, G. K. 1991, ApJ, 370, 78, doi: [10.1086/169794](https://doi.org/10.1086/169794)
- Hopkins, P. F., Kereš, D., Oñorbe, J., et al. 2014, MNRAS, 445, 581, doi: [10.1093/mnras/stu1738](https://doi.org/10.1093/mnras/stu1738)
- Ji, S., Oh, S. P., & Masterson, P. 2019, MNRAS, 487, 737, doi: [10.1093/mnras/stz1248](https://doi.org/10.1093/mnras/stz1248)
- Kanjilal, V., Dutta, A., & Sharma, P. 2021, MNRAS, 501, 1143, doi: [10.1093/mnras/staa3610](https://doi.org/10.1093/mnras/staa3610)
- Klein, R. I., McKee, C. F., & Colella, P. 1994, ApJ, 420, 213, doi: [10.1086/173554](https://doi.org/10.1086/173554)
- Kolmogorov, A. 1941, Akademiia Nauk SSSR Doklady, 30, 301
- Krumholz, M. R., & Kruijssen, J. M. D. 2015, MNRAS, 453, 739, doi: [10.1093/mnras/stv1670](https://doi.org/10.1093/mnras/stv1670)
- Larson, R. B. 1981, MNRAS, 194, 809, doi: [10.1093/mnras/194.4.809](https://doi.org/10.1093/mnras/194.4.809)
- Li, Z., Hopkins, P. F., Squire, J., & Hummels, C. 2020, MNRAS, 492, 1841, doi: [10.1093/mnras/stz3567](https://doi.org/10.1093/mnras/stz3567)
- Mac Low, M.-M. 1999, ApJ, 524, 169, doi: [10.1086/307784](https://doi.org/10.1086/307784)
- Maller, A. H., & Bullock, J. S. 2004, MNRAS, 355, 694, doi: [10.1111/j.1365-2966.2004.08349.x](https://doi.org/10.1111/j.1365-2966.2004.08349.x)
- Marquardt, D. W. 1963, Journal of the Society for Industrial and Applied Mathematics, 11, 431, doi: [10.1137/0111030](https://doi.org/10.1137/0111030)
- Mo, H. J., & Miralda-Escude, J. 1996, ApJ, 469, 589, doi: [10.1086/177808](https://doi.org/10.1086/177808)
- Muratov, A. L., Kereš, D., Faucher-Giguère, C.-A., et al. 2015, MNRAS, 454, 2691, doi: [10.1093/mnras/stv2126](https://doi.org/10.1093/mnras/stv2126)
- Nelson, D., Vogelsberger, M., Genel, S., et al. 2013, MNRAS, 429, 3353, doi: [10.1093/mnras/sts595](https://doi.org/10.1093/mnras/sts595)
- Nielsen, N. M., Churchill, C. W., Kacprzak, G. G., Murphy, M. T., & Evans, J. L. 2015, ApJ, 812, 83, doi: [10.1088/0004-637X/812/1/83](https://doi.org/10.1088/0004-637X/812/1/83)
- Ossenkopf, V., & Mac Low, M. M. 2002, A&A, 390, 307, doi: [10.1051/0004-6361/20020629](https://doi.org/10.1051/0004-6361/20020629)
- Ostriker, E. C., Gammie, C. F., & Stone, J. M. 1999, ApJ, 513, 259, doi: [10.1086/306842](https://doi.org/10.1086/306842)
- Ostriker, E. C., Stone, J. M., & Gammie, C. F. 2001, ApJ, 546, 980, doi: [10.1086/318290](https://doi.org/10.1086/318290)
- Rubin, K. H. R., Prochaska, J. X., Koo, D. C., et al. 2014, ApJ, 794, 156, doi: [10.1088/0004-637X/794/2/156](https://doi.org/10.1088/0004-637X/794/2/156)
- Rudie, G. C., Steidel, C. C., Trainor, R. F., et al. 2012, ApJ, 750, 67, doi: [10.1088/0004-637X/750/1/67](https://doi.org/10.1088/0004-637X/750/1/67)
- Schneider, E. E., Ostriker, E. C., Robertson, B. E., & Thompson, T. A. 2020, ApJ, 895, 43, doi: [10.3847/1538-4357/ab8ae8](https://doi.org/10.3847/1538-4357/ab8ae8)
- Shen, S., Madau, P., Guedes, J., et al. 2013, ApJ, 765, 89, doi: [10.1088/0004-637X/765/2/89](https://doi.org/10.1088/0004-637X/765/2/89)
- Sparre, M., Pfrommer, C., & Ehlert, K. 2020, MNRAS, 499, 4261, doi: [10.1093/mnras/staa3177](https://doi.org/10.1093/mnras/staa3177)
- Stern, J., Fielding, D., Faucher-Giguère, C.-A., & Quataert, E. 2020, MNRAS, 492, 6042, doi: [10.1093/mnras/staa198](https://doi.org/10.1093/mnras/staa198)
- Stern, J., Faucher-Giguère, C.-A., Fielding, D., et al. 2021, ApJ, 911, 88, doi: [10.3847/1538-4357/abd776](https://doi.org/10.3847/1538-4357/abd776)
- Stocke, J. T., Keeney, B. A., Danforth, C. W., et al. 2013, ApJ, 763, 148, doi: [10.1088/0004-637X/763/2/148](https://doi.org/10.1088/0004-637X/763/2/148)
- Stone, J. M., & Norman, M. L. 1992a, ApJS, 80, 753, doi: [10.1086/191680](https://doi.org/10.1086/191680)
- . 1992b, ApJS, 80, 791, doi: [10.1086/191681](https://doi.org/10.1086/191681)
- Stone, J. M., Ostriker, E. C., & Gammie, C. F. 1998, ApJL, 508, L99, doi: [10.1086/311718](https://doi.org/10.1086/311718)
- Tenorio-Tagle, G., & Muñoz-Tuñón, C. 1998, MNRAS, 293, 299, doi: [10.1046/j.1365-8711.1998.01194.x](https://doi.org/10.1046/j.1365-8711.1998.01194.x)
- Tenorio-Tagle, G., Silich, S., Rodríguez-González, A., & Muñoz-Tuñón, C. 2005, ApJL, 628, L13, doi: [10.1086/432665](https://doi.org/10.1086/432665)
- Thompson, T. A., Quataert, E., Zhang, D., & Weinberg, D. H. 2016, MNRAS, 455, 1830, doi: [10.1093/mnras/stv2428](https://doi.org/10.1093/mnras/stv2428)
- Tumlinson, J., Peeples, M. S., & Werk, J. K. 2017, ARA&A, 55, 389, doi: [10.1146/annurev-astro-091916-055240](https://doi.org/10.1146/annurev-astro-091916-055240)
- Vazza, F., Brunetti, G., Kritsuk, A., et al. 2009, A&A, 504, 33, doi: [10.1051/0004-6361/200912535](https://doi.org/10.1051/0004-6361/200912535)
- Voit, G. M. 2018, ApJ, 868, 102, doi: [10.3847/1538-4357/aae8e2](https://doi.org/10.3847/1538-4357/aae8e2)
- Voit, G. M., Meece, G., Li, Y., et al. 2017, ApJ, 845, 80, doi: [10.3847/1538-4357/aa7d04](https://doi.org/10.3847/1538-4357/aa7d04)
- Werk, J. K., Prochaska, J. X., Thom, C., et al. 2013, ApJS, 204, 17, doi: [10.1088/0067-0049/204/2/17](https://doi.org/10.1088/0067-0049/204/2/17)
- Werk, J. K., Prochaska, J. X., Tumlinson, J., et al. 2014, ApJ, 792, 8, doi: [10.1088/0004-637X/792/1/8](https://doi.org/10.1088/0004-637X/792/1/8)
- Werk, J. K., Prochaska, J. X., Cantalupo, S., et al. 2016, ApJ, 833, 54, doi: [10.3847/1538-4357/833/1/54](https://doi.org/10.3847/1538-4357/833/1/54)
- White, S. D. M., & Rees, M. J. 1978, MNRAS, 183, 341, doi: [10.1093/mnras/183.3.341](https://doi.org/10.1093/mnras/183.3.341)
- Xu, J., & Stone, J. M. 1995, ApJ, 454, 172, doi: [10.1086/176475](https://doi.org/10.1086/176475)
- Yang, Y., & Ji, S. 2023, MNRAS, 520, 2148, doi: [10.1093/mnras/stad264](https://doi.org/10.1093/mnras/stad264)
- Zahedy, F. S., Chen, H.-W., Johnson, S. D., et al. 2019, MNRAS, 484, 2257, doi: [10.1093/mnras/sty3482](https://doi.org/10.1093/mnras/sty3482)

Zhang, Y.-T., Shi, J., Shu, C.-W., & Zhou, Y. 2003, Phys. Rev. E, 68, 046709, doi: [10.1103/PhysRevE.68.046709](https://doi.org/10.1103/PhysRevE.68.046709)